

Ari Alastalo

Microelectromechanical Resonator-Based Components for Wireless Communications

| Filters and Transmission Lines

Microelectromechanical Resonator- Based Components for Wireless Communications

Filters and Transmission Lines

Ari Alastalo

*Dissertation for the degree of Doctor of Science in Technology
to be presented with due permission of the Department of Engineering Physics
and Mathematics for public examination and debate in Large Seminar Hall of
Micronova at Helsinki University of Technology (Espoo, Finland)
on the 1st of November, 2006, at 12 o'clock noon.*



ISBN 951-38-6865-6 (soft back ed.)

ISSN 1235-0621 (soft back ed.)

ISBN 951-38-6866-4 (URL: <http://www.vtt.fi/publications/index.jsp>)

ISSN 1455-0849 (URL: <http://www.vtt.fi/publications/index.jsp>)

Copyright © VTT Technical Research Centre of Finland 2006

JULKAISIJA – UTGIVARE – PUBLISHER

VTT, Vuorimiehentie 3, PL 2000, 02044 VTT

puh. vaihde 020 722 111, faksi 020 722 4374

VTT, Bergsmansvägen 3, PB 2000, 02044 VTT

tel. växel 020 722 111, fax 020 722 4374

VTT Technical Research Centre of Finland, Vuorimiehentie 3, P.O.Box 2000, FI-02044 VTT, Finland

phone internat. +358 20 722 111, fax + 358 20 722 4374

VTT, Tietotie 3, PL 1000, 02044 VTT

puh. vaihde 020 722 111, faksi 020 722 7012

VTT, Datavägen 3, PB 1000, 02044 VTT

tel. växel 020 722 111, fax 020 722 7012

VTT Technical Research Centre of Finland, Tietotie 3, P.O. Box 1000, FI-02044 VTT, Finland

phone internat. +358 20 722 111, fax +358 20 722 7012

Alastalo, Ari. Microelectromechanical Resonator-Based Components for Wireless Communications. Filters and Transmission Lines [Mikromekaanisiin resonaattoreihin perustuvat komponentit langattoman tiedonsiirron sovelluksissa. Suodattimet ja siirtolinjat]. Espoo 2006. VTT Publications 616. 57 p. + app. 56 p.

Keywords MEMS, radio-frequency MEMS, microelectromechanical filters, microelectromechanical resonators, components, transducers, wireless communication, transmission lines, acoustic wave propagation, intermodulation

Abstract

Starting in the early 1960's, when the integrated-circuit (IC) technology was developed, micromachining and microelectromechanical systems (MEMS) have grown into a broad research field with several commercial successes. Typical applications of MEMS are in physical, chemical and biochemical sensors, as well as in optical systems such as the digital micromirror device of Texas Instruments. From the 1990's, the advances in the processing technologies and the tremendous growth of the wireless-communication market have drawn much interest into radio-frequency MEMS devices (RF MEMS) such as filters, oscillators, switches and tunable capacitors. These are now beginning to penetrate the market.

This thesis considers electrostatically-actuated RF-MEMS filters and delay lines. For filters, the work concentrates on nonlinear distortion and filter design. The intermodulation properties of capacitively-coupled MEMS filters are analytically solved in closed form and the theory is verified in numerical simulations as well as in measurements with MEMS resonators. The analysis is more generally valid than the previously published results. The theory is utilized to formulate a design procedure for MEMS filters that, for the first time, takes systems specifications for tolerable intermodulation distortion and insertion-loss into account. For delay lines, capacitive actuation of bulk-acoustic waves in a solid rod is analyzed. In particular, challenges in impedance matching due to the weakness of the electrostatic coupling are quantified. Finally, a new kind of resonator-chain delay line for high-frequency (HF) signals is introduced. This delay line is characterized by extremely slow signal group velocity ($\sim 10\text{--}100$ m/s), narrow-band response, and much lower characteristic impedance than found for the solid-rod waveguide enabling efficient signal coupling. Properties of the resonator-chain waveguide are theoretically analyzed and the results are verified in measurements of fabricated devices.

Alastalo, Ari. Microelectromechanical Resonator-Based Components for Wireless Communications. Filters and Transmission Lines [Mikromekaanisiin resonaattoreihin perustuvat komponentit langattoman tiedonsiirron sovelluksissa. Suodattimet ja siirtolinjat]. Espoo 2006. VTT Publications 616. 57 s. + liitt. 56 s.

Avainsanat MEMS, radio-frequency MEMS, microelectromechanical filters, microelectromechanical resonators, components, transducers, wireless communication, transmission lines, acoustic wave propagation, intermodulation

Tiivistelmä

Mikroelektromekaanisten järjestelmien (MEMS) kehitys alkoi 1960-luvun alussa yhdessä integroitujen piirien (IC) teknologian kanssa. Tähän päivään mennessä mikromekaanikka on kehittynyt laajaksi tutkimusalaksi ja johtanut useisiin kaupallisiin menestyksiin. MEMS-teknologiaa sovelletaan mm. fysikaalisissa, kemiallisissa ja biokemiallisissa antureissa sekä optisissa järjestelmissä, kuten Texas Instrumentsin mikropileissä, joita käytetään videoprojektoreissa. Kiinnostus radiotaajuisiin MEMS- komponentteihin (RF MEMS) on lisääntynyt voimakkaasti 1990-luvun alusta alkaen valmistusteknologian ja langattoman tiedonsiirron markkinoiden kehityksen myötä. Radiotekniikassa MEMS-teknologiaa pyritään soveltamaan mm. suodattimissa, oskillaattoreissa, kytkimissä ja säädettävissä kondensaattoreissa. Ensimmäiset tällaiset komponentit ovat jo kaupallistuneet.

Tässä väitöskirjassa käsitellään kapasitiivisesti kytkettyjä RF-MEMS-suodattimia ja viivelinjoja. Suodattimien osalta työ keskittyy epälineaarisuuksien ja häviöiden huomioimiseen suodinsuunnittelussa. MEMS-suodinten intermodulaatio-ominaisuudet ratkaistaan työssä analyttisesti aikaisempaa yleisemmin ja saadut tulokset varmennetaan tietokonesimulaatioissa ja mittauksissa. Tulosten pohjalta laaditaan MEMS-suodinsuunnittelulle säännöt, joissa otetaan ensimmäistä kertaa huomioon asetetut vaatimukset sekä intermodulaatiolle että häviöille. Viivelinjojen osalta työssä käsitellään mikromekaaniseen tankoon perustuvaa tilavuusaaltoviivelinjaa ja tuodaan esiin vaikeudet, jotka liittyvät riittävän hyvän kytkennän saavuttamiseen tällaisessa rakenteessa. Tehokkaampi kytkentä on HF-taajuuksilla mahdollinen jousimassaketjuun perustuvaan viivelinjaan, jollainen esitellään ja analysoidaan tässä väitöstyössä. Hyvän kytkennän lisäksi tämän viivelinjan ominaisuuksiin kuuluu kapeakaistaisuus ja erittäin hidas signaalin kulkunopeus. Mikromekaanisen jousimassaketjuviivelinjan toiminta varmennetaan mittauksin.

Preface

Research for this dissertation was done at the Microsensing Laboratory of VTT Information Technology during 2002–2005. The work was done in close collaboration with several colleagues at Microsensing, the Microelectronics Centre and the Radiotechnology group of VTT as well as with many co-workers in the Materials Physics Laboratory, SMARAD Radio Laboratory, Metrology Research Institute and Circuit Theory Laboratory of Helsinki University of Technology (TKK).

Funding from VTT in the Future Communication Technologies strategic technology theme for the MEMS radio project and from the Academy of Finland in the Future Electronics Research Programme (TULE) for the MIRA project was indispensable to the research work and is gratefully acknowledged. I am also thankful to the Jenny and Antti Wihuri Foundation, the Academy of Finland and VTT for financial support during 2006 to finalize the thesis.

I am deeply indebted to my instructor Prof. Heikki Seppä and to the manager of Microsensing Dr. Timo Varpula for an opportunity to work in the field of RF MEMS and for guidance in the research work. They have, together with all the personnel, managed to create and maintain excellent working conditions and fruitful and open atmosphere in Microsensing. In particular, the inexhaustible ideas of Prof. Seppä are invaluable in stimulating brainstorming to find directions and to meet challenges of research. I am most thankful to my supervisors Prof. Martti Salomaa, whose dedicated guidance was deprived from his students by his untimely death in 2004, and to Prof. Matti Kaivola, who has greatly facilitated the final stages of the work. Insightful comments of Dr. Tapani Ryhänen and Dr. Remco Wiegerink were also of valuable help in writing the overview. In addition, I have been privileged to collaborate with Professors Antti Räisänen, Ilkka Tittonen, Aarne Oja and Markku Åberg.

I wish to express my gratitude to the many co-workers at VTT and TKK that I have been fortunate to work with during the years. Especially, technical discussions with Doc. Tomi Mattila and Dr. Ville Kaajakari have been most beneficial. Somehow, they have always found time to share their insight. Special thanks go to Dr. James Dekker and Dr. Jyrki Kiihamäki for outstanding work in MEMS fabrication that enabled the experiments of the thesis. Discussions and collaboration with as well as help and support of a large number of people, including Mika Koskenvuori, Jan Holmberg, Hannu Salminen, Markku Jenu, Dr. Tauno Vähä-Heikkilä, Dr. Timo Veijola, Dr. Jouni Knuuttila, Pekka Rantakari, Mikko Kiviranta, Anu Kärkkäinen, Dr. Jukka Kyynäräinen, Paula Holmlund, Jari Penttilä, Anssi Rautiainen, Ari Häärä, Dr. Kari Leppänen, Seija Lepistö, Aija Kaski and Kaisa Falenius, are also thankfully acknowledged.

My warm thanks go to my parents Maire and Reijo and to my brother Petri for support and presence in the many good things of life. Finally, the greatest of my thanks belong to my dear wife Hanna and to my wonderful son Aaro for bringing value and joy to each day.

List of Publications

This thesis is based on the following original publications. Other related publications by the author are cited in the text [1–4].

Intermodulation Distortion in MEMS Filters:

- I Ari T. Alastalo and Ville Kaajakari, “Intermodulation in Capacitively Coupled Microelectromechanical Filters,” *IEEE Electron Device Letters*, vol. 26, no. 5, pp. 289–291, May 2005.
- II Ari T. Alastalo and Ville Kaajakari, “Third-Order Intermodulation in Microelectromechanical Filters Coupled with Capacitive Transducers,” *IEEE Journal of Microelectromechanical Systems*, vol. 15, no. 1, pp. 141–148, February 2006.
- III Ari T. Alastalo and Ville Kaajakari, “Systematic Design Approach for Capacitively Coupled Microelectromechanical Filters,” *IEEE Transactions on Ultrasonics, Ferroelectrics, and Frequency Control*, vol. 53, no. 9, pp. 1662–1670, September 2006.

Acoustic Transmission Lines:

- IV Ari T. Alastalo, Tomi Mattila, and Heikki Seppä, “Analysis of a MEMS Transmission Line,” *IEEE Transactions on Microwave Theory and Techniques*, vol. 51, no. 8, pp. 1977–1981, August 2003.
- V Ari T. Alastalo, Tomi Mattila, Heikki Seppä, and James Dekker, “Micromechanical slow-velocity delay lines,” *Proc. 33rd European Microwave Conference*, Munich, Germany, 6–10 October, 2003, pp. 967–970.
- VI Ari T. Alastalo, Jyrki Kiihamäki, and Heikki Seppä, “Microelectromechanical delay lines with slow signal propagation,” *Journal of Micromechanics and Microengineering*, vol. 16, pp. 1854–1860, August 2006.

In the text, these publications are referred to by their Roman numerals.

Author’s Contribution

The author has done all the theoretical analysis, characterization of the MEMS components, numerical simulations and measurements of all the contributed publications I–VI. He has also been responsible of writing of all the papers and has contributed most of the text of I–V and all of VI. The author has designed the MEMS components used in V and VI. In addition, the author has presented the results of the work at international conferences including the European Microwave Conference in Munich (Germany) 2003 and the IEEE International Ultrasonics Symposium in Rotterdam (The Netherlands) 2005.

Contents

Abstract	3
Tiivistelmä	4
Preface	5
List of Publications	6
Abbreviations	8
Symbols and Notation	9
1 Introduction	11
1.1 MEMS in Radio Architectures	12
1.2 Mechanical Resonators	14
1.3 Electrostatic Transduction in MEMS	16
1.4 SOI MEMS Fabrication at VTT	19
1.4.1 Standard VTT MEMS Process	19
1.4.2 Fabrication Process for Narrow Gaps	20
1.5 Nonlinearities in Signal-Processing Applications	21
1.6 Objectives of the Work	24
2 Designing MEMS Filters for RF Applications	25
2.1 Filtering with a Single Resonator	25
2.2 Multi-Stage Filters	27
2.3 IM3 for MEMS Filters	27
2.4 Generalization of the IM3 Theory	31
2.5 Design Principles of MEMS Filters	33
2.6 Design Example	34
3 Acoustic Transmission Lines	38
3.1 Bulk-Wave Waveguides	38
3.2 Resonator Chains	39
3.2.1 Measurements of Test Structures	43
3.2.2 Minimizing the Characteristic Impedance	43
4 Discussion on Frequency Scaling	46
5 Conclusions	47
References	49
Appendices	
1 Electromechanical Instability	
2 Derivation of the Equivalent Circuits	
3 Publications I–VI	

Abbreviations

VTT	Technical Research Centre of Finland
TKK	Helsinki University of Technology
ETSI	European Telecommunications Standards Institute
GSM	global system for mobile communications (an ETSI standard)
RFID	radio-frequency identification
RX	radio receiver
TX	radio transmitter
IC	integrated circuit
FET	field-effect transistor
LNA	low-noise amplifier
MEMS	microelectromechanical systems
SOI	silicon on insulator
LTO	low-temperature oxide
CVD	chemical vapor deposition
RIE	reactive-ion etch
DRIE	deep reactive-ion etch (Bosch process)
ICP	inductively-coupled plasma
SAW	surface-acoustic wave
BAW	bulk-acoustic wave
FBAR	film-bulk-acoustic resonator
RF	radio frequency
IF	intermediate frequency of a superheterodyne receiver
HF	high frequency (3–30 MHz) (hydrofluoric acid in fabrication)
VHF	very high frequency (30–300 MHz)
UHF	ultra high frequency (300 MHz–3 GHz)
IM3	third-order intermodulation
IP3	third-order intercept point
IIP3	input-referred third-order intercept point
SIR	signal-to-intermodulation ratio
C/I	carrier-to-interference ratio

Symbols and Notation

ϵ_0	vacuum permittivity	$8.85419 \times 10^{-12} \text{ F/m}$
ρ	density	
Y	Young's modulus	
\dot{y}	time derivative of variable y	
\ddot{y}	second time derivative of variable y	
q	charge	
φ	electrostatic potential	
U	voltage	
V	bias voltage	
V_{pi}	pull-in voltage	
u	AC source voltage	
\bar{u}	normalized AC voltage (small)	$= u/V$
C	capacitance	
E	capacitor energy	$= \frac{1}{2}CU^2$
A	area of a capacitive transducer	
x	transducer or resonator displacement	
d	transducer gap with $x = 0$	
ξ	normalized transducer displacement (small)	$= x/d$
C_0	transducer capacitance with $x = 0$	$= \epsilon_0 A/d$
Z_0	transducer impedance with $x = 0$	$= 1/(j\omega C_0)$
η	electromechanical coupling	$= C_0 V/d$
k_e	electromechanical spring constant	$= \eta V/d$
k	spring constant of a harmonic resonator	
m	resonator mass	
γ	resonator damping constant	
Q	resonator quality factor	$= \sqrt{km}/\gamma$
ω_0	resonator eigenfrequency	$= \sqrt{k/m}$
$H(\omega)$	resonator response function	$= H'(\omega) + jH''(\omega)$
ω_e	electromechanical frequency	$= \sqrt{k_e/m}$
\bar{k}	spring constant with capacitive coupling	$= k - 2k_e$
$\bar{\omega}_0$	eigenfrequency with capacitive coupling	$= \sqrt{\bar{k}/m}$
\bar{Q}	quality factor with capacitive coupling	$= \sqrt{\bar{k}m}/\gamma$
R_m	electrical-equivalent resonator resistance	$= \gamma/\eta^2$

L_m	electrical-equivalent resonator inductance	$= m/\eta^2$
C_m	electrical-equivalent resonator capacitance	$= \eta^2/\bar{k}$
Z_L	load impedance	
R_L	load resistance	
C_L	load capacitance	
R_{ac}	source resistance	
R'_S	series-equivalent source resistance	
C'_S	series-equivalent source capacitance	
R'_L	series-equivalent load resistance	
C'_L	series-equivalent load capacitance	
γ'	loaded resonator dissipation constant	$= \eta^2 (R_m + R'_S + R'_L)$
k'	loaded resonator spring constant	$= \eta^2 \left(\frac{1}{C_m} + \frac{1}{C'_S} + \frac{1}{C'_L} \right)$
Q'	loaded resonator Q value	$= \sqrt{k'm}/\gamma'$
ω'	loaded resonator eigenfrequency	$= \sqrt{k'/m}$
u'	Thévenin-equivalent-source AC voltage	$= u/(1 + j\omega C_0 R_{ac})$
P_{IIP3}	input power corresponding to IIP3	
P_{1dB}	input power for to 1-dB compression	
Γ_{III}	ratio of third harmonic to fundamental	
Γ	interference to signal ratio	
Γ_{int}	amplitude ratio of interferers	
G_V	voltage gain	
k_c	coupling spring of a resonator chain	
k_a	anchoring spring of a resonator chain	
m_0	coupling mass of a resonator chain	
a	period of a resonator chain	
ω_s	frequency of a symmetric eigenmode of a two-mode resonator	
ω_a	frequency of an antisymmetric eigenmode of a two-mode resonator	
K	ratio of anchoring spring to coupling spring	$= k_a/k_c$
M	total coupled-resonator mass	$= 2m + m_0$
λ	wavelength	
κ	wavevector	$= 2\pi/\lambda$
v_g	group velocity	
v_{ph}	phase velocity	
Z_c	characteristic impedance of a transmission line	

1 Introduction

Acoustic wave propagation in solids has for a long time been utilized in RF electronics to implement various functionalities in components such as local oscillators, filters, and delay lines. Such devices are based on transduction between electric signals and acoustic waves with part of the signal processing being performed in the mechanical domain. In these applications, one benefits from i) low attenuation of acoustic waves in crystalline materials and ii) low acoustic wave velocity compared to electromagnetic waves. The low attenuation enables high Q values of mechanical resonators in components such as quartz-based oscillators [5] that are widely used as low-phase-noise frequency references in mobile-communication devices. The low-loss propagation is also essential in surface-acoustic-wave (SAW) and bulk-acoustic-wave (BAW or FBAR) filters [6, 7]. The acoustic SAW and BAW velocities are of the order of 5000 m/s that is approximately 10^5 times smaller than the wave velocities for electromagnetic transmission lines. Thus, long signal delays can be produced with small-sized components. This is utilized, for example, in the SAW radio-frequency-identification (RFID) tags.

Recent advances in MEMS technology have opened up the possibility for creating micro-sized RF devices based on mechanical motion. In MEMS, integrated-circuit (IC) batch-fabrication technologies are utilized to produce miniature mechanical structures usually on a silicon substrate. As an example, a MEMS plate resonator has been demonstrated to be well suited for a high-spectral-purity oscillator in mobile-communication applications with phase-noise properties comparable to its quartz-based counterparts [8]. MEMS variable capacitors and, especially, switches are the most studied RF MEMS components with commercial products now on sale by a few companies [9]. MEMS switches are also utilized, for example, in phase shifters and impedance tuners [10, 11]. Micromechanical filters are at present studied as a potential technology for bandpass filtering in receiver front ends either at RF or IF frequencies [12–16]. Replacement of the conventional SAW and FBAR filters with MEMS that is integrable with CMOS electronics can reduce the cost, power consumption and physical size of the RF circuitry. This becomes more and more important as the number of different radios in a single device is increasing. Sometimes, also stationary components fabricated with MEMS technology, such as inductors and waveguides, are considered as a part of RF MEMS. For recent review articles and books on RF MEMS, see [9, 10, 17–20] and [21, 22], respectively. Besides in RF applications, MEMS technology is utilized, for example, in sensors, such as accelerometers, gyroscopes, magnetometers and pressure sensors, as well as in microfluidic devices and in micromirrors for projection displays (see, for example, [23, 24]).

This thesis considers design and analysis of electrostatically-actuated micro-acoustic RF filters and delay lines fabricated with MEMS technology for radio-communication devices. After the introduction to microelectromechanical systems in Chapter 1, the thesis focuses on the new scientific results of the work. In

Chapter 2, intermodulation (IM) properties of capacitively-coupled MEMS filters are analytically solved and the theory is verified in numerical simulations as well as in measurements. Although MEMS filters are widely studied in the literature, IM has received less attention. The new theory is utilized to formulate a design procedure for MEMS filters that takes both IM and insertion-loss requirements into account. Usage of the procedure is exemplified and implications of the analysis for different receiver architectures are discussed. MEMS delay lines are considered in Chapter 3. First, capacitive actuation of bulk-acoustic waves in a solid rod is analyzed. In particular, challenges in impedance matching due to the weakness of the electrostatic coupling are quantified. Then, a new kind of resonator-chain delay line for HF-frequency signals is introduced. This delay line is characterized by extremely slow signal group velocity, narrow-band response, and much lower characteristic impedance than found for the solid-rod waveguide enabling efficient signal coupling. Properties of the resonator-chain waveguide are theoretically analyzed and verified in simulations and measurements. Conclusions of the work are presented in Chapter 5.

1.1 MEMS in Radio Architectures

MEMS-based components have been suggested to implement many of the needed functionalities in modern communication devices. To set the context of the thesis more clearly, a typical superheterodyne radio architecture is depicted in Fig. 1 [25]. The blue shading indicates components that can possibly be realized with MEMS technology. In addition to the switches, phase shifters, local oscillators, filters and impedance tuners that are generally recognized as potential applications of MEMS [8–11, 15, 20–22], for the power sensor, used in the radio of Fig. 1 to control the power amplifier (PA), one can consider using MEMS, as first discussed in [26] and developed further, for example, in [2, 27].

Instead of developing MEMS replacements of conventional components, full utilization of the properties of MEMS may well require a redesign of the overall architecture and may prove well suited also for low-power low-performance radios of wireless sensors. Namely, MEMS may allow some of the different operations of Fig. 1 to be performed in a single electromechanical device, such as the RX front-end filtering, mixing and even the low-noise amplification using parametric pumping [1, 28]. In [15, 29], an architecture is considered, where the RX-band-select filter is replaced with a switchable bank of narrow-band filters with different center frequencies to cover the RX band. With such an approach, the linearity requirements of the LNA and the mixer can be relaxed due to the introduced selectivity against in-channel interferences. A multitude of parallel channel-select filters is also considered in [30] with FBAR filters for a radio of wireless sensors. Instead of many parallel filters, one can also consider using a single multimode MEMS resonator, such as the plate resonator of [8] with Lamé and square-extensional modes, if the size of the radio is to be minimized.

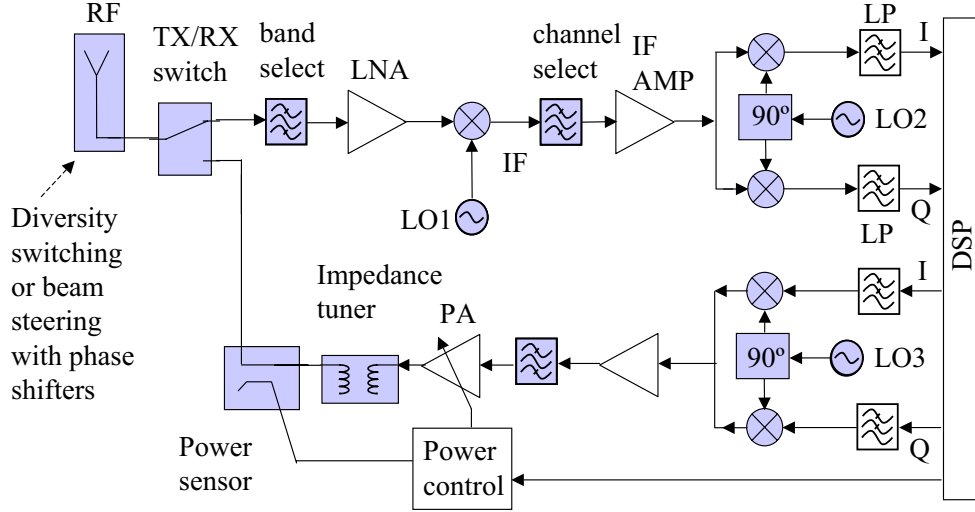


Figure 1: Superheterodyne radio architecture. Components for which MEMS implementation can be considered are indicated in blue.

Figure 2 schematically shows another possible architecture for a low-power radio transponder terminal that communicates with a high-power basestation. Here the TX carrier is generated from the RX signal using a time delay during which the TX/RX switch changes its state. The carrier generation can comprise, for example, a phase-lock loop or, if the basestation is sending an unmodulated carrier for the terminal TX, passband filtering can be enough. With a narrow-band delay line, the filters in Fig. 2 can possibly be omitted. SAW RFID tags are an example of a transponder radio, where the input RX pulse is coupled to a delay line with multiple reflectors that cause many TX pulses, with identifiable inter-pulse delays, to be sent back.

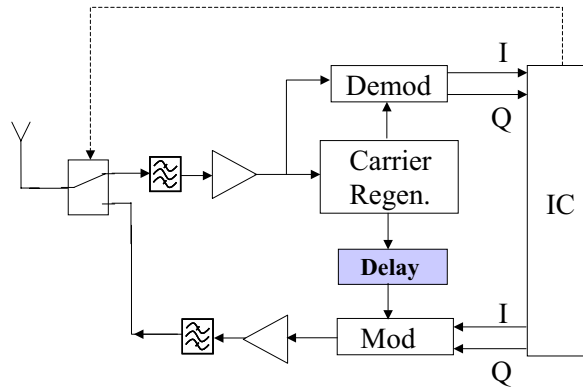


Figure 2: Schematic of a radio-transponder architecture where the delay line is used to separate reception and transmission in time.

1.2 Mechanical Resonators

Typical mechanical resonator geometries are shown in Fig. 3. The applied force, F , either stretches (a) or bends (b) the beam or stretches the plate (c) that is anchored to ideally undeformable supports. For small amplitudes at and close to the resonance frequency, the resonators can be modelled with a linear spring-mass system, as shown in Fig. 3 (d), for which the equation of motion is

$$m\ddot{x} + \gamma\dot{x} + kx = F \Leftrightarrow \ddot{x} + \frac{\omega_0}{Q}\dot{x} + \omega_0^2 x = F/m \equiv \bar{F}. \quad (1)$$

Here $\omega_0 = \sqrt{k/m}$ is the eigenfrequency and $Q = \sqrt{km}/\gamma$ is the quality factor of the resonator with spring constant, k , mass, m , and dissipation, γ . The dots above the variables refer to derivation with respect to time. Solution to (1) can conveniently be written using the complex response function

$$H(\omega) \equiv \left(\omega_0^2 - \omega^2 + j\frac{\omega\omega_0}{Q} \right)^{-1} \quad (2)$$

as

$$x(\omega) = \bar{F}H' + \dot{\bar{F}}H''/\omega, \quad (3)$$

where H' and H'' denote the real and imaginary parts of H , respectively. The second term in (3), which is proportional to the first time derivative of the applied force, describes the power dissipation of the system. The absolute value of the response

$$|H| = \sqrt{H'^2 + H''^2} = \left[(\omega_0^2 - \omega^2)^2 + (\omega\omega_0/Q)^2 \right]^{-1/2} \quad (4)$$

gives the amplitude, x_0 , of the displacement, x , as $x_0 = |H|\bar{F}_0$, where \bar{F}_0 is the scaled amplitude of the applied force.

For large amplitudes, nonlinearities of the resonator have to be taken into account. Spring nonlinearities can be included in (1) by replacing the linear spring force with a nonlinear force as

$$kx \rightarrow kx + k_2x^2 + k_3x^3 + \dots \quad (5)$$

Taking the nonlinear terms into account only up to the third order, the equation of motion (1) becomes

$$\ddot{x} + \frac{\omega_0}{Q}\dot{x} + \omega_0^2 x + \alpha x^2 + \beta x^3 = \bar{F}, \quad (6)$$

where $\alpha \equiv k_2/m$ and $\beta \equiv k_3/m$. The higher-order terms (αx^2 and βx^3) in (6) introduce a shift to the resonance frequency, $\omega_r \equiv \omega_0 + \omega_\delta$, and tilt the response of the resonator [31, 32] (Duffing effect). The resonance frequency shift, ω_δ , as a function of the resonator amplitude, x_0 , is given by

$$\omega_\delta = \delta x_0^2, \quad (7)$$

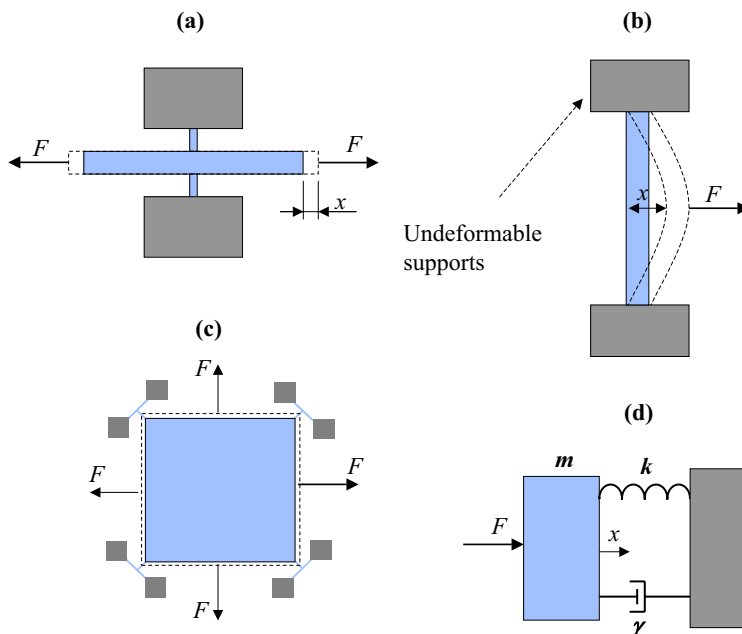


Figure 3: Typical resonator geometries, (a) stretching beam (b) bending beam and (c) extending plate of [8]. The resonators are anchored to stationary supports. (d) For small motion close to the resonance frequency, the resonators can be modelled with a linear spring-mass system (harmonic oscillator).

where [31, 32]

$$\delta = \frac{3\beta}{8\omega_0} - \frac{5\alpha^2}{12\omega_0^3}. \quad (8)$$

At the critical resonance amplitude of

$$x_{0,c} = \frac{2\sqrt{\omega_0}}{\sqrt{3Q|\delta|\sqrt{3}}}, \quad (9)$$

the response becomes a multivalued function of frequency with two stable and one unstable solution for each excitation frequency resulting in hysteresis [31, 32]. The amplitude responses of the linear ($\delta = 0$) and some nonlinear resonators are schematically shown in Fig. 4. The nonlinear responses have been obtained by considering a unit-amplitude force ($\bar{F}_0 = 1$) and solving for the resonator amplitude, x_0 , in (4) after substitutions $|H| = x_0$ and $\omega_0 \rightarrow \omega_r = \omega_0 + \delta x_0^2$. The behaviour of the response in hysteresis is also indicated.

The resonator geometries of Fig. 3 are typical in RF MEMS filters [12, 13, 15, 33] and oscillators [8, 34, 35]. Other state-of-the-art MEMS resonators have been based, for example, on tuning forks, [36], folded-beams [15], ring [37] or circular disk [38, 39] geometry. The highest frequency- Q products of microresonators have been reported for a silicon ring [37] and a diamond disk [40] ($Q > 10\,000$

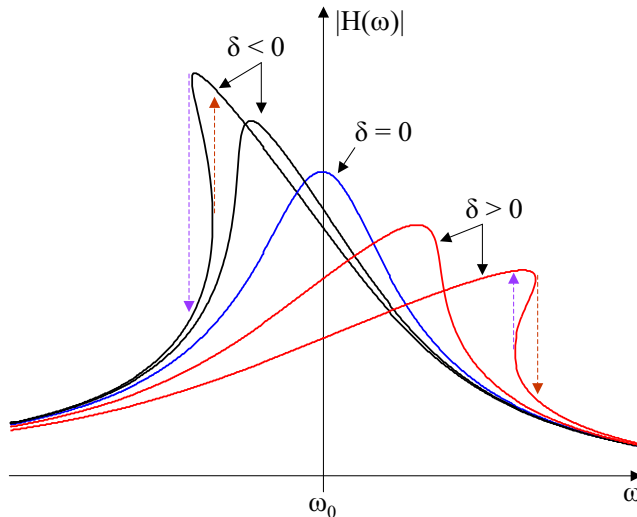


Figure 4: Tilting of the resonator response due to nonlinearity. The dashed arrows show the behaviour of the solution with hysteresis, when the frequency ω of the excitation force is increased (red) or lowered (blue).

at $f \sim 1$ GHz). Research is also in progress towards reducing the size of the resonators below one micrometer [41, 42]. Compared to MEMS, utilization of these submicron nanomechanical (NEMS) devices in RF systems is much more challenging due to their more complicated fabrication and inefficient coupling to electric signals.

1.3 Electrostatic Transduction in MEMS

Several choices exist for coupling electrical signals and mechanical motion [21, 43]. In microsystems, most common is the electrostatic actuation due to its low power consumption, fast operation and simplicity of the needed fabrication processes [21, 22]. The most studied RF application of MEMS is an RF switch [22] (for recent references, see also [44–46]) for which capacitive coupling typically suffers from high actuation voltages (high, at least, for battery-powered applications) and inadequate reliability due to dielectric charging [22]. Therefore, for MEMS switches, one has also utilized piezoelectric [47] and magnetic [48] transducers, as well as combinations of magnetic and electrostatic [49] and of thermal and electrostatic transducers [50].

Capacitively actuated MEMS resonators have been demonstrated at up to GHz frequencies [37, 39]. However, achieving good enough signal coupling becomes increasingly challenging as the device size shrinks with increasing resonance frequency. Consequently, higher bias voltages and smaller transducer gaps are needed. Alternatively, piezoelectric coupling has been used also for MEMS resonators [51–54] as well as electromagnetic [55], magnetostrictive [56] and ther-

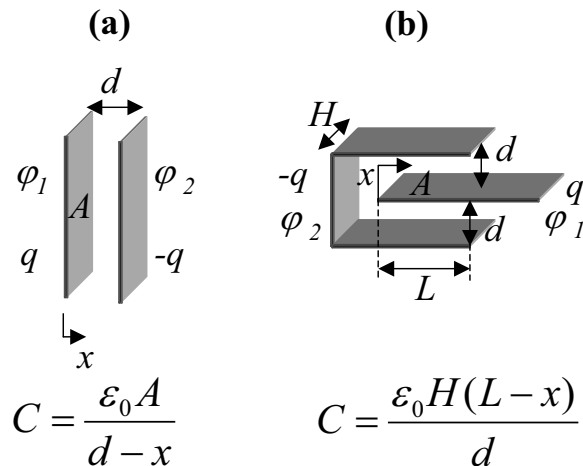


Figure 5: Conductors at potentials φ_1 and φ_2 with charges q and $-q$, respectively, forming the parallel-plate (a) and comb-drive (b) capacitive transducers. The conductor plate with charge q is movable and its displacement with respect to the initial position is denoted with x .

mal [57] transducers. Electrostatic transducers with high-permittivity dielectrics replacing the air gap have also recently been introduced [14, 58, 59] and analyzed in detail in [4]. While offering solutions to the problems of electrostatic actuation, the other approaches have their own challenges [21] such as demanding or expensive fabrication (permanent magnets and current coils or piezoelectric or magnetostrictive thin films), slow operation (thermal transducers) and power consumption (thermal and magnetic transducers). In what follows, this thesis concentrates on capacitive coupling.

Two common electrostatic transducers, parallel plate and comb drive, are shown in Fig. 5. The actual comb drive is composed of several elements of the type in Fig. 5 (b) in parallel [60], but here it suffices to consider only a single element. The transducer capacitors are composed of two conductor plates at potentials φ_1 and φ_2 with charges q and $-q$, respectively. One of the plates is movable and its displacement with respect to the initial position is denoted with x . Energy stored in the transducers is

$$E = \frac{1}{2}CU^2 = \frac{1}{2}\frac{q^2}{C}, \quad (10)$$

where $U \equiv \varphi_2 - \varphi_1$ is the voltage difference between the conductors and C is the transducer capacitance given in Fig. 5. With biasing, either the voltage, U , or the charge, q , is kept constant, resulting in a force between the conductor plates

as [61]

$$F = \left. \frac{\partial E}{\partial x} \right|_U = \frac{1}{2} U^2 \frac{\partial C}{\partial x} \quad (\text{voltage bias}) \quad (11 \text{ a})$$

$$F = - \left. \frac{\partial E}{\partial x} \right|_q = - \frac{1}{2} q^2 \frac{\partial}{\partial x} \left(\frac{1}{C} \right) \quad (\text{charge bias}). \quad (11 \text{ b})$$

Consequently, with voltage biasing, the force (11 a) is a nonlinear function of the displacement, x , for the parallel-plate transducer of Fig. 5 (a) while for the comb drive of Fig. 5 (b), the force does not depend on x . Vice versa, with charge biasing, the force (11 b) is independent of x for the parallel-plate transducer and a nonlinear function of x for the comb-drive.

Due to its simple implementation and applicability also in the presence of significant parasitic capacitances [62], such as pad capacitances, voltage biasing has been the preferred solution in RF MEMS applications. Furthermore, although the comb drive results in better linearity properties, better coupling (stronger force) can be obtained with the parallel-plate transducer by minimizing the electrode gap. Good coupling is critical, for example, in MEMS filters to minimize the insertion loss. In the following, only voltage-biased parallel-plate transducers are considered.

One effect of the nonlinearity of the voltage-biased parallel-plate transducer is that when applied to the mechanical resonators of Fig. 3 at high enough bias voltages, the resonators become unstable and are deflected against the stationary electrodes. This effect, called pull-in, can be utilized, for example, in MEMS switches [21] and sensors [26] but must be avoided in RF filters, thus setting an upper limit for the bias voltage (pull-in voltage). With the transducer forces as indicated in Fig. 3, the pull-in voltage is

$$V_{\text{pi},1} = \sqrt{\frac{8kd^2}{27C_0}}, \quad (12 \text{ a})$$

where C_0 is the transducer capacitance with $x = 0$. With two transducers placed on both sides of the resonator of Fig. 3 (b), such that the bias forces act in opposite directions, the pull-in occurs at a higher voltage of

$$V_{\text{pi},2} = \sqrt{\frac{kd^2}{2C_0}}. \quad (12 \text{ b})$$

In addition, using the two transducers as a differential drive (voltage $V + u$ on one transducer and $V - u$ on the other, where V is the bias voltage and u a small signal) the second-order signal nonlinearity can be reduced. To the third-order nonlinearities that are in focus in this thesis, the differential drive has no effect. Appendix 5 outlines the derivation of (12 a) and (12 b). Since the rest position of the resonator with symmetric biasing for $V < V_{\text{pi},2}$ is at $x = 0$, the effective spring constant, $\bar{k} = k - 2k_e$, vanishes at the pull-in voltage.

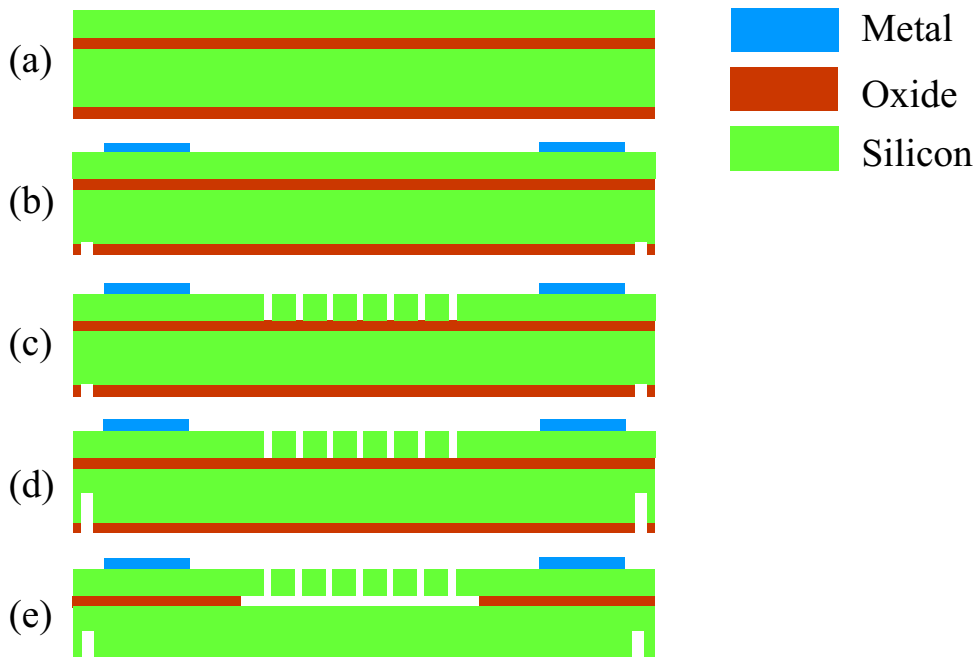


Figure 6: Basic MEMS device fabrication process. (a) Oxide deposition, (b) metallization, (c) device patterning, (d) sawline etching, (e) device releasing.

1.4 SOI MEMS Fabrication at VTT

The silicon-on-insulator (SOI) fabrication processes used at VTT for the components characterized in this thesis are outlined in what follows. More detailed discussions on silicon-based MEMS surface, bulk and SOI micromachining can be found, for example, in [63–65]. Present research also focuses on use of i) diamond for the highest quality factors and two times higher sound velocity than in silicon (higher frequencies with the same resonator dimensions) [40,66], ii) silicon carbide for somewhat higher sound velocity with similar fabrication technologies as for silicon [67,68] and iii) silicon germanium to facilitate post-CMOS integration due to its low thermal budget [38,69]. Diamond and silicon carbide are also considered to be more suitable than silicon for environments with demanding thermal, chemical, radiation or wear conditions [70].

1.4.1 Standard VTT MEMS Process

Fabrication of the devices described in Publication V is illustrated in Fig. 6. The process makes use of a SOI wafer which contains a $1\text{-}\mu\text{m}$ buried oxide layer beneath a $10\text{-}\mu\text{m}$ silicon device layer. After depositing an extra $1\text{-}\mu\text{m}$ -thick low-temperature-oxide (LTO) layer on the wafer backside with chemical vapor deposition (CVD) (a), metal is deposited using Argon (Ar) plasma and patterned on the front side (b). The metallization consists of a titanium-tungsten (TiW) dif-

fusion barrier, a 1- μm -thick aluminum (Al) layer, and a thin molybdenum (Mo) top layer to protect the Al against the hydrofluoric acid (HF) that is later used for release etch. Etching of the metal is carried out using either a chlorine-based ($\text{Cl}_2 + \text{BCl}_3 + \text{CHCl}_3$) reactive-ion-etch (RIE) RF plasma or by wet etching. A short dip in Freckle etchant is used to remove the residual etch debris. Sawing lines are then patterned on the backside oxide layer and etched a few microns deep with $\text{CF}_4 + \text{CHF}_3$ -based RIE plasma. The next step (c) is the patterning of the resonator structures, with nominal gaps of 0.5 μm , and release holes of 1.5 μm diameter. Inductively-coupled plasma (ICP) is used in the Bosch process [64, 71] with $\text{SF}_6 + \text{C}_4\text{F}_8$ -etch and $\text{C}_4\text{F}_8 + \text{Ar}$ -passivation steps to form the gaps and release holes using a resist mask, which is then stripped in oxygen plasma before the backside sawlines are etched to a greater depth (d), again using ICP etching but with the previously patterned oxide as a mask. The Bosch process is also called deep reactive-ion etch (DRIE). The buried oxide (and the backside LTO) is then etched for several minutes in 49% HF and then dried in supercritical CO_2 (e). The devices may be separated by cleaving along the sawlines or by sawing.

1.4.2 Fabrication Process for Narrow Gaps

Table 1: Clamped-clamped (CC) beam, free-free (FF) beam and square-plate resonators with narrow transducer gaps.

gap / [nm]	type	dimensions	f / [MHz]	Q	Ref.
200	CC beam	3.7 $\mu\text{m} \times 54 \mu\text{m}$	8	5400	[72]
100	FF beam	2 $\mu\text{m} \times 40 \mu\text{m}$	10	10000	[73]
80	CC beam	3 $\mu\text{m} \times 200 \mu\text{m}$	0.6	4800	[74]
60	CC beam	3 $\mu\text{m} \times 30 \mu\text{m}$	30	2500	[75]
50	square plate	320 $\mu\text{m} \times 320 \mu\text{m}$	13	4000	[76]

In order to obtain good-enough coupling with low-enough bias voltages for capacitively-coupled RF MEMS resonators, several processes have been developed to minimize the transducer gap. Resonators with vertical gaps of $d \approx 200$ nm [72], $d \approx 100$ nm [73], $d \approx 80$ nm [74], $d \approx 60$ nm [75] and $d \approx 50$ nm [76] have been fabricated. Relevant properties of these resonators are summarized in Table 1. In [76], a much higher quality factor of $Q > 10^5$ is found for a resonator with otherwise the same parameter values but with the transducer gap increased to $d \approx 180$ nm. For [75], the effective gap, given by the bias-voltage dependence of the resonance frequency, is found to be $d \approx 400$ nm, which is suggested to be caused by carrier depletion. In [72, 73, 75], the reported quality factors for the beam resonators are in good agreement with the support-loss estimate of $Q < 2(L/w)^2$ [77]. For [74, 76], on the other hand, the low quality factors of

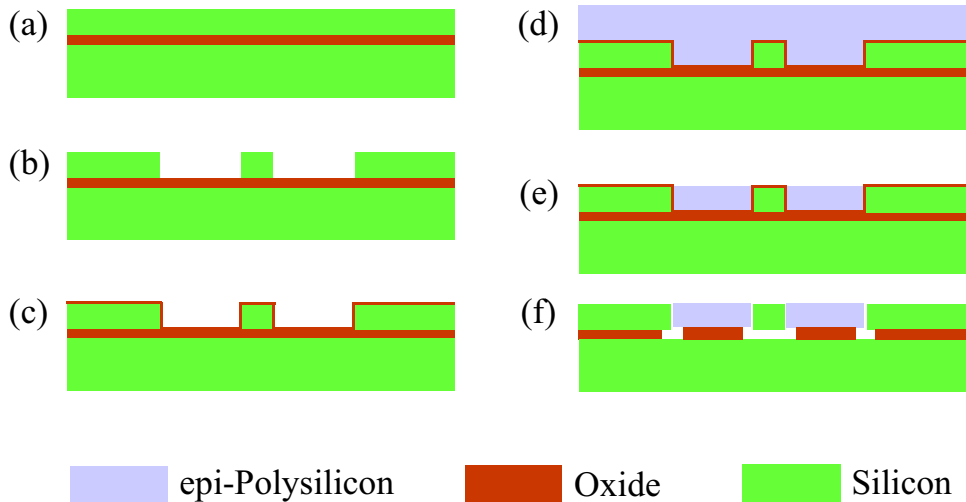


Figure 7: VTT MEMS process for narrow-gap devices. (a) SOI starting wafer, (b) etching of electrode areas with DRIE (Bosch process), (c) deposition of sacrificial oxide, (d) epitaxial polycrystalline-silicon deposition, (e) grinding and polishing, (f) device releasing.

the sub-100-nm-gap resonators can be explained neither by anchoring loss [77] nor by thermoelastic damping [78] but are possibly due to surface effects [77] or contamination [76] in the narrow gaps.

The narrow-gap processes [72–76] are based on a deposition of a thin sacrificial layer of oxide or polysilicon to define the gaps. Figure 7 illustrates the process developed at VTT [76] that is used for the devices characterized in Publications I, II and VI. The electrode areas are first etched in the Bosch process (b) after which a thin sacrificial layer of thermal oxide (c), and a layer of epitaxial polycrystalline silicon (d) are deposited on the wafer. Next, grinding and silicon-selective chemical-mechanical polishing (CMP) are used to bring the structural layer back to its original thickness (e). Finally, HF etch (f) is used to release the vibrating structures. The process can be finalized with a wafer-level vacuum sealing step as discussed in [76].

1.5 Nonlinearities in Signal-Processing Applications

After the above introduction of capacitively-coupled MEMS resonators as well as their mechanical (5) and electrical (11 a) sources of nonlinearity, typical figures of merit of linearity, used in signal-processing applications, are discussed in what follows for future reference. Noise properties of MEMS resonators [79–81] that also are of central importance in signal processing are left outside the scope of this work.

Typically, for a narrow transducer gap, the capacitive nonlinearity is the dom-

inant source of distortion. Odd-order nonlinearities are especially detrimental as they can lead to unwanted frequency components at a desired-signal frequency, ω_0 . For example, cubic mixing of two fundamental signals, having frequencies ω_1 and ω_2 , results in third-order intermodulation (IM3) products at frequencies $2\omega_1 - \omega_2$ and $2\omega_2 - \omega_1$. This is easily seen [82] with a signal

$$x_{\text{in}} = A_1 \cos \omega_1 t + A_2 \cos \omega_2 t \quad (13)$$

at the input of a nonlinear system for which the response can be modelled as a third-order polynomial

$$x_{\text{out}} = \alpha_0 + \alpha_1 x_{\text{in}} + \alpha_2 x_{\text{in}}^2 + \alpha_3 x_{\text{in}}^3. \quad (14)$$

Here we ignore any nonlinearities of higher than third order, although, in practise, they can also be important. Inserting (13) to (14), one obtains

$$\begin{aligned} x_{\text{out}} = & \frac{1}{4} [\alpha_0 + 2\alpha_2 A_1^2 + 2\alpha_2 A_2^2 + \\ & + (\boxed{4\alpha_1 A_1} + 3\alpha_3 A_1^3 + \overline{6\alpha_3 A_1 A_2^2}) \cos(\omega_1 t) + \\ & + (4\alpha_1 A_2 + 3\alpha_3 A_2^3 + \overline{6\alpha_3 A_1^2 A_2}) \cos(\omega_2 t) + \\ & + 2\alpha_2 A_1^2 \cos(2\omega_1 t) + \alpha_3 A_1^3 \cos(3\omega_1 t) + \\ & + 2\alpha_2 A_2^2 \cos(2\omega_2 t) + \alpha_3 A_2^3 \cos(3\omega_2 t) + \\ & + 4\alpha_2 A_1 A_2 \cos(\omega_1 t - \omega_2 t) + 4\alpha_2 A_1 A_2 \cos(\omega_1 t + \omega_2 t) + \\ & + \boxed{3\alpha_3 A_1^2 A_2} \cos(2\omega_1 t - \omega_2 t) + 3\alpha_3 A_1 A_2^2 \cos(2\omega_2 t - \omega_1 t) + \\ & + 3\alpha_3 A_1^2 A_2 \cos(2\omega_1 t + \omega_2 t) + 3\alpha_3 A_1 A_2^2 \cos(\omega_1 t + 2\omega_2 t)] . \end{aligned} \quad (15)$$

The boxed, underlined and overlined terms of (15) are referred to in what follows. If $\omega_1 = \omega_0 + \Delta\omega$ and $\omega_2 = \omega_0 + 2\Delta\omega$, the IM3 product at $2\omega_1 - \omega_2$ is at ω_0 corrupting the desired signal at that frequency. In the following, we introduce the commonly used measures of nonlinearity: third-order intercept point, 1-dB compression and harmonics.

Third-Order Intercept Point: The third-order intercept point (IP3) is typically defined as the crossing point of the linear extrapolations of the small-amplitude IM3 signal at $2\omega_1 - \omega_2$ and a fundamental two-tone test signal at ω_1 or ω_2 (with $A_1 = A_2$) in the device output. The signal level at the input, corresponding to IP3, is termed IIP3. Setting the boxed amplitudes in (15) equal, one obtains for the IIP3 amplitude $A_{\text{IIP3}}^2 = 4|\alpha_1|/(3|\alpha_3|)$ [82]. Using the same boxed terms of (15) but the first one for a desired signal, $x_{\text{sig}} = A_{\text{sig}} \cos(\omega_0 t)$, and the second one for interference (13) with $A_1 = A_2 = A_{\text{int}}$, one finds for the signal-to-intermodulation ratio (SIR) at the output of the system

$$\text{SIR} = A_{\text{IIP3}}^2 \frac{A_{\text{sig}}}{A_{\text{int}}^3} = P_{\text{IIP3}} \sqrt{\frac{P_{\text{sig}}}{P_{\text{int}}^3}}, \quad (16)$$

where the last result is expressed in terms of the signal and interference powers at the input. The result (16) is valid also for frequency selective components, such as filters, provided that the IP3 definition is modified as being the crossing point of the linear extrapolations of the IM3 output signal and a wanted output signal when the wanted signal has the same input magnitude as the interferers and is located at the passband center.

1-dB Compression: Typically, the coefficient α_3 for the third-order term in (14) is negative and thus the gain of the system decreases for increasing signal amplitudes as seen in the amplitude of the $\cos(\omega_1 t)$ term in (15). The 1-dB compression point is defined as the input signal level for which the gain has decreased by 1 dB. The corresponding amplitude, $A_{1\text{dB}}$, can be solved using the underlined terms in (15) ($A_2 = 0$). The linear gain for the signal with amplitude A_1 is α_1 while the compressed gain is $\alpha_1 + \frac{3}{4}\alpha_3 A_1^2$. Thus $A_{1\text{dB}}$ is found by solving [82]

$$20 \log \left| \alpha_1 + \frac{3}{4}\alpha_3 A_{1\text{dB}}^2 \right| = 20 \log |\alpha_1| - 1 \text{ dB}. \quad (17)$$

Consequently, in terms of powers, one finds a useful relation between the intercept point and compression

$$P_{1\text{dB}} \approx P_{\text{IIP3}} - 10 \text{ dB}. \quad (18)$$

If $A_2 \gg A_1$, gain for the weaker signal follows from the overlined terms in (15) and the compression point is found as in (17) but with the $\frac{3}{4}$ replaced with $\frac{3}{2}$. One finds

$$\hat{P}_{1\text{dB}} \approx P_{\text{IIP3}} - 13 \text{ dB}, \quad (19)$$

where $\hat{P}_{1\text{dB}}$ denotes the power level at which gain for a much weaker signals is reduced by 1 dB.

Harmonics: The amplitudes of the second and third harmonics ($x_{\text{out}}^{\text{II}}$ and $x_{\text{out}}^{\text{III}}$) with respect to the fundamental term ($x_{\text{out}}^{\text{I}}$) are also easily obtained from (15). In particular, one finds that the third harmonic can be related to P_{IIP3} as

$$\Gamma_{\text{III}} \equiv 20 \log_{10} \left(\frac{x_{\text{out}}^{\text{III}}}{x_{\text{out}}^{\text{I}}} \right) = 2 (P_1 - P_{\text{IIP3}}) - 10 \text{ dB}, \quad (20)$$

where P_1 is the power corresponding to the signal amplitude A_1 . For example, for the GSM mobile terminal with maximum transmit power of 33 dBm, it is required that the third harmonics in TX remain below -30 dBm [83]. Consequently, ignoring antenna and switch losses, one needs for the power P_{IIP3} , according to (20), $P_{\text{IIP3}} > 60$ dBm. With the switch losses and the antenna efficiency taken into account, the minimum acceptable P_{IIP3} is accordingly raised.

1.6 Objectives of the Work

The objective of the work is to contribute to the progress of reducing the size, price and power consumption (increased operation time of battery-powered devices) of communication systems by wider utilization of MEMS components. Both replacement of components, such as filters, in conventional radios and devices enabling novel radio architectures are to be considered. The research questions of the work are:

- 1) In order to use capacitive MEMS resonators for front-end filters in wireless radio receivers as suggested, for example, in [15], what are the requirements for the central parameter values such as supply voltage, transducer gap and resonator quality factor?
- 2) What are the possible obstacles of commercially using MEMS resonators for filtering at UHF frequencies?
- 3) How to systematically design MEMS filters to meet filter specifications of a communication system such as GSM [83], concentrating, in particular, on intermodulation distortion [84] and on insertion loss?
- 4) What are the central tradeoffs in filter properties that affect the design?
- 5) Instead of replacing conventional RF components with MEMS devices, can more be gained through a redesign of the radio architecture? What special requirements do MEMS filters set for the overall system?
- 6) How can low-loss acoustic propagation in single-crystal silicon be used for novel time-delay components and delay-line radio architectures?

2 Designing MEMS Filters for RF Applications

In radio systems, micromechanical filters have been suggested for bandpass filtering in the receiver front ends either at RF or IF frequencies. In contrast to conventional acoustic SAW and FBAR filters that pass the entire RX band, their MEMS replacements are often thought to have a narrower passband. This is enabled by the high quality factors of MEMS resonators that are achievable by utilizing low-loss single-crystal materials and vacuum packaging. For example, capacitively-actuated MEMS resonators with quality factors of $Q > 100\,000$ at 10 MHz [8] and $Q > 10\,000$ at 1 GHz [37] have been reported. Consequently, one needs tuning of the filter passband or a bank of switchable filters with different center frequencies to cover all the RX channels of the communication system as discussed in [15] and in Sec. 1.1. A central challenge of MEMS filters is to obtain a low-enough mechanical impedance for acceptable insertion loss. Consequently, for bias voltages that are practical for mobile devices, maximizing the resonator quality factor and minimizing the transducer gap become of primary interest although they increase the nonlinear distortion of the device. In this thesis, a filter design approach that takes both insertion-loss and intermodulation-distortion requirements into account is developed.

2.1 Filtering with a Single Resonator

Usage of a mechanical resonator, with mass, m , spring constant, k , and dissipation constant, γ , as a bandpass filter for capacitively-coupled electrical signals with voltage bias is schematically shown in Fig. 8. The load impedance is denoted by Z_L , the source impedance by R_{ac} and $Z = u/i_1$ is the small-signal impedance seen when looking into the input transducer. The resonator mass is grounded and the bias voltage, V , is connected to the mechanically stationary electrodes of the parallel-plate transducers. The transducer area is A and d is the width of the gap with the resonator at its rest position. As the resonator mass is displaced by x , the transducer capacitances become

$$C_1 = \frac{C_0}{1 + x/d} = C_0 [1 - \xi + \xi^2 - \xi^3 + \dots] \quad (21\text{ a})$$

$$C_2 = \frac{C_0}{1 - x/d} = C_0 [1 + \xi + \xi^2 + \xi^3 + \dots], \quad (21\text{ b})$$

where $C_0 = \epsilon_0 A/d$ is the rest capacitance ($x = 0$) and $\xi \equiv x/d$ is the normalized displacement. With the electromechanical coupling coefficient defined as $\eta \equiv C_0 V/d$ and the spring constant as $k_e \equiv \eta V/d$, the small-signal electrical-equivalent

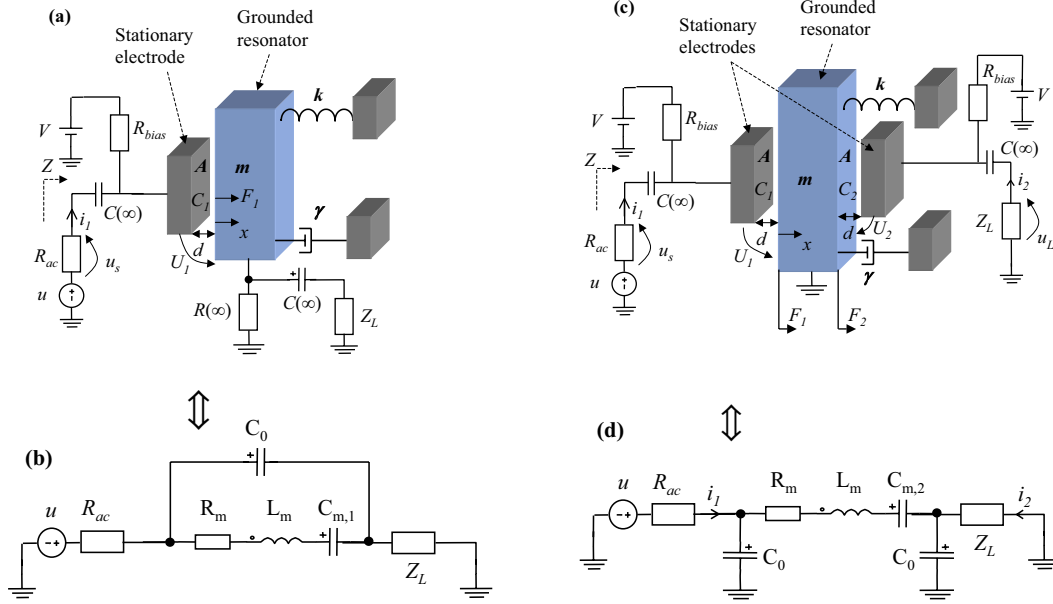


Figure 8: Micromechanical resonator operating as a single-stage band-pass filter for capacitively-coupled signals with unsymmetric (a) and symmetric (c) bias. In (b) and (d), the corresponding electrical-equivalent small-signal models are shown.

parameters in Fig. 8 (b) and (d) are found as [16, 43]

$$R_m = \frac{\gamma}{\eta^2} \quad (22 \text{ a})$$

$$L_m = \frac{m}{\eta^2} \quad (22 \text{ b})$$

$$C_{m,N} = \frac{\eta^2}{k - Nk_e}, \quad (22 \text{ c})$$

where N is the number of transducers ($N = 1$ in Fig. 8 (a,b) and $N = 2$ in Fig. 8 (c,d)). With these definitions, the coupling coefficient, η , is included in the values of the equivalent resistance, inductance and capacitance. Alternatively, the coupling can be modelled with a transformer [43]. In App. 5, details of the derivation of the equivalent circuits are explained. With only one transducer ($N = 1$), the transducer area can be larger than for $N = 2$ resulting in a better electromechanical coupling and lower R_m . For example, for the plate resonator of Fig. 3 (c), all the four faces can be used for actuation. However, as in filtering and delay-line applications it is important to eliminate the direct electrical signal propagation through C_0 between the input and output ports, it is better to use two capacitive transducers ($N = 2$), one for input and one for output, and connect the resonator to AC ground potential as shown in Fig. 8 (c, d). Consequently, in what follows, we mainly concentrate on the two-transducer approach of Fig. 8 (c, d).

Forces F_1 and F_2 in Fig. 8, exerted on the moving mass, are found with (11 a) as

$$F_1 = -\frac{1}{2} U_1^2 \frac{C_0/d}{(1+\xi)^2} = -\frac{1}{2} (V+u-u_s)^2 \frac{C_0}{d} [1-2\xi+3\xi^2-4\xi^3+\dots] \quad (23 \text{ a})$$

$$F_2 = \frac{1}{2} U_2^2 \frac{C_0/d}{(1-\xi)^2} = \frac{1}{2} (V-u_L)^2 \frac{C_0}{d} [1+2\xi+3\xi^2+4\xi^3+\dots]. \quad (23 \text{ b})$$

Here U_i are the voltages across the transducers ($U_1 = V+u-u_s$ and $U_2 = V-u_L$), $u_s = i_1 R_{ac}$ is the voltage drop in the source resistance and $u_L = i_2 Z_L$ is the load voltage as indicated in Fig. 8. The currents i_1 and i_2 in Fig. 8 (c,d) are

$$i_1 = \frac{dQ_1}{dt} = \frac{d(C_1 U_1)}{dt} = C_1(\dot{u} - \dot{u}_s) + (V+u-u_s) \frac{\partial C_1}{\partial x} \dot{x} \quad (24 \text{ a})$$

$$i_2 = \frac{dQ_2}{dt} = \frac{d(C_2 U_2)}{dt} = -C_2 \dot{u}_L + (V-u_L) \frac{\partial C_2}{\partial x} \dot{x}, \quad (24 \text{ b})$$

where the derivatives of the capacitances are the same as for the forces in (23 a) and (23 b). Equations (23 a)–(24 b) and the equation of motion of the resonator form the basis of the calculations in this thesis.

2.2 Multi-Stage Filters

Multistage MEMS filters can be composed, for example, by coupling resonators in series with mechanical springs [15, 16], by using shunt capacitors or active buffers [12] or by using direct capacitive coupling between the resonators [13]. The spring coupling [15, 16] has the same electrical-equivalent representation as the shunt-capacitance-coupled filter [12] which is shown in Fig. 9 for two stages. Here C_{gnd} is the inter-stage coupling capacitor.

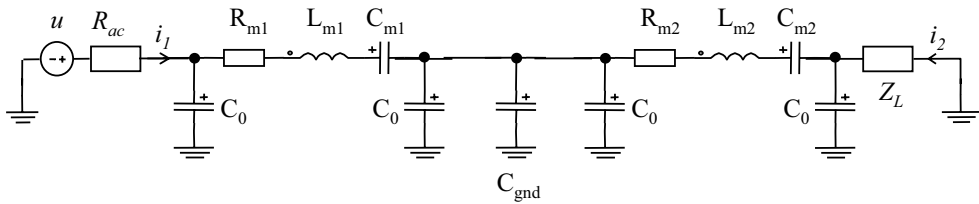


Figure 9: A two-stage MEMS filter where the inter-stage coupling is done with the shunt capacitance C_{gnd} .

2.3 IM3 for MEMS Filters

The intermodulation properties of capacitively-coupled single-resonator MEMS filters are solved in closed form in Publications I–II and the theory is generalized

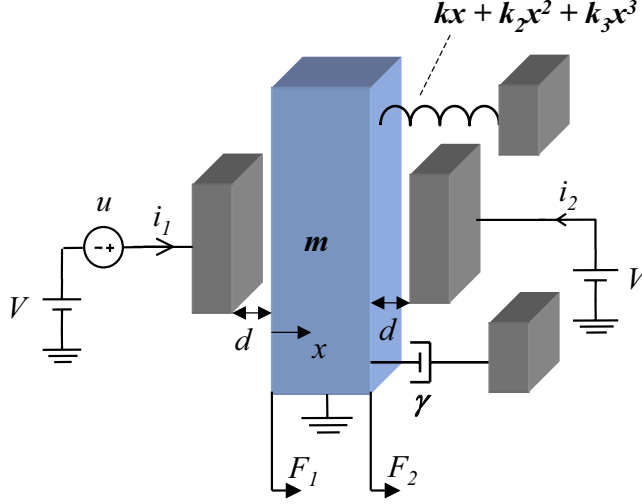


Figure 10: Filter circuit of Fig. 8 (c) simplified for intermodulation analysis.

for higher-order filters in Publication III and [3]. We consider the circuit of Fig. 8 (c) with $R_{ac} = Z_L = 0$ as shown in Fig. 10. Nonzero source and load impedances will be included afterwards as done in Publication III. Furthermore, for generality we include mechanical spring nonlinearities up to third order with (5). The equation of motion of the resonator in Fig. 10 up to third order in the small parameters, $\bar{u} \equiv u/V$ and $\xi \equiv x/d$, is found with the forces of (23 a) and (23 b) as

$$\ddot{\xi} + \frac{\bar{\omega}_0}{\bar{Q}} \dot{\xi} + \bar{\omega}_0^2 \xi = -\omega_e^2 \left[\bar{u} + \bar{k}_2 \xi^2 - 2\bar{u}\xi + \frac{\bar{u}^2}{2} - (4 - \bar{k}_3) \xi^3 + 3\bar{u}\xi^2 - \bar{u}^2 \xi \right] = \bar{F}. \quad (25)$$

Here, the following definitions are used: $\bar{\omega}_0 \equiv \sqrt{\bar{k}/m}$, $\bar{Q} \equiv \sqrt{\bar{k}m}/\gamma$, $\omega_e \equiv \sqrt{k_e/m}$, $\bar{k}_2 \equiv dk_2/k_e$ and $\bar{k}_3 \equiv d^2k_3/k_e$ with $\bar{k} \equiv k - 2k_e$, $k_e \equiv \eta V/d$ and $\eta \equiv C_0 V/d$. The output current is found from (24 b) as

$$\bar{i} \equiv \frac{i_2}{d} = \eta \left(\underset{\bar{i}_{\text{sig}}, \bar{i}_{\text{IM3}}^{(1)}}{1 + 2\xi + 3\xi^2} + \underset{\bar{i}_{\text{IM3}}^{(2)}}{4\xi^3 + \dots} \right) \dot{\xi}. \quad (26)$$

In (26), we have indicated the terms that contribute to the signal and the intermodulation currents at the fundamental frequency, $\bar{\omega}_0$.

The desired signal, \bar{u}_{sig} , at the resonance frequency, $\bar{\omega}_0$, and an interfering signal, \bar{u}_{int} , at the filter input are now taken as

$$\bar{u}_{\text{sig}} = \bar{u}_{\text{sig},0} \cos \bar{\omega}_0 t, \quad (27a)$$

$$\bar{u}_{\text{int}} = \bar{u}_{\text{int},0} (\cos \omega_1 t + \Gamma_{\text{int}} \cos \omega_2 t), \quad (27b)$$

where $\omega_1 \equiv \bar{\omega}_0 + \Delta\omega$ and $\omega_2 \equiv \bar{\omega}_0 + 2\Delta\omega$ such that a third-order intermodulation product of (27b) is at the desired-signal frequency, $\bar{\omega}_0$. The frequency separation of the interferers is denoted by $\Delta\omega$. A possible difference in the interferer amplitudes is taken into account with Γ_{int} .

The output signal current, \bar{i}_{sig} , in (26) is found by first obtaining the linear signal motion, ξ_{sig} , from (3) with a force, \bar{F}_{sig} , given by the excitation (27a) in (25) as $\bar{F}_{\text{sig}} = -\omega_e^2 \bar{u}_{\text{sig}}$. Similarly, linear resonator motion, ξ_{int} , at the interferer frequencies, ω_1 and ω_2 , is found from (3) with a force, \bar{F}_{int} , given by (27b) in (25) as $\bar{F}_{\text{int}} = -\omega_e^2 \bar{u}_{\text{int}}$. The intermodulation currents, $\bar{i}_{\text{IM3}}^{(1)}$ and $\bar{i}_{\text{IM3}}^{(2)}$, in (26) at $\bar{\omega}_0$ due to the interference (27b) are obtained in Publication II by approximately solving the nonlinear equation of motion (25).

The signal-to-intermodulation ratio (SIR), defined as the ratio of the signal current, \bar{i}_{sig} , to the total intermodulation current, $\bar{i}_{\text{IM3}} = \bar{i}_{\text{IM3}}^{(1)} + \bar{i}_{\text{IM3}}^{(2)}$, is given in Publication II for a general case. For practical usage in filter design, it is more convenient to consider SIR in the limit of $\bar{Q} \rightarrow \infty$ that becomes valid as soon as the interferers are well outside the passband of the filter. We find

$$\text{SIR}_{\bar{Q} \rightarrow \infty} = \frac{16|\Delta\omega|^3(\bar{\omega}_0 + \Delta\omega)(2\bar{\omega}_0 + \Delta\omega)^2}{\left[9\Delta\omega^4 + 28\Delta\omega^3\bar{\omega}_0 + 2\Delta\omega^2(10\bar{\omega}_0^2 - 9\omega_e^2) + \right.} \quad (28)$$

$$\left. - 24\Delta\omega\omega_e^2\bar{\omega}_0 + 3(4 - \bar{k}_3)\omega_e^4\right]\Gamma_{\text{int}}\Gamma^3\bar{u}_{\text{sig},0}^2\omega_e^2}$$

where $\Gamma \equiv \bar{u}_{\text{int},0}/\bar{u}_{\text{sig},0}$ is the interference-to-signal ratio at the filter input. As (28) contains odd powers of $\Delta\omega$, it is asymmetric around the resonance predicting different SIR values for interferers below the resonance and interferers above the resonance.

Another important limit is when the interferers are inside the filter passband ($\Delta\omega \rightarrow 0$). This is relevant, for example, when signal self distortion is considered. In terms of the IIP3 voltage, we have with $\Gamma_{\text{int}} = 1$ (Publication I)

$$\bar{u}_{0,\text{IIP3,IB}}^2 = 1 / \sqrt{[3(1 - \bar{k}_3/4)p^3 + p/4]^2 + 9p^4/4}, \quad (29)$$

where $p \equiv \bar{Q}\omega_e^2/\bar{\omega}_0^2 = k_e\bar{Q}/\bar{k}$. The corresponding SIR is found from (16).

The theoretical results are compared to measurements and numerical simulations in Publication II. A good accuracy of the theory is found as shown, for example, in figure 11 for the square-extensional-mode plate resonator of Fig. 3 (c). The resonator is fabricated on a silicon-on-insulator (SOI) wafer with the narrow-gap process of [76] (see Sec. 1.4.2) and it has a size of $320 \mu\text{m} \times 320 \mu\text{m} \times 10 \mu\text{m}$ (thickness of the SOI device layer is $10 \mu\text{m}$). For other details, see Publication II. For signal input and output, two parallel capacitive transducers on opposite sides of the plate are used. Each transducer corresponds to one of the four forces shown in Fig. 3 (c). For example, for input, the transducers are on the left- and on the right-hand side of the plate while the output transducers are

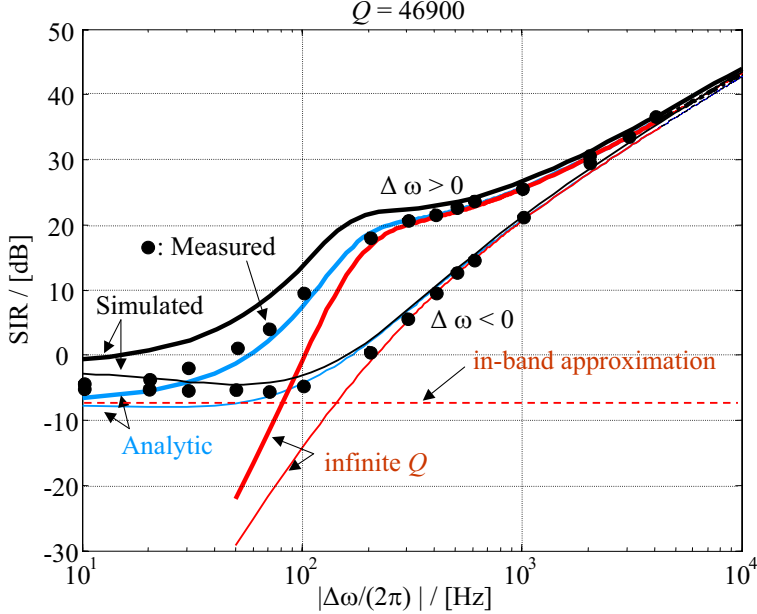


Figure 11: Signal-to-intermodulation ratio as a function of interferer frequency separation for the square-plate resonator of Publication II that is schematically illustrated in Fig. 3 (c). Simulated behaviour (black curves), general analytic result of Publication II (blue curves), analytic result in the limit $\bar{Q} \rightarrow \infty$ (28) (red curves), in-band limit (29) (dashed line), and measured results (large dots) are shown. The thin curves are for $\Delta\omega < 0$ while the thick curves are for $\Delta\omega > 0$.

located below and above the plate. A bias voltage is brought to the stationary transducer electrodes while the resonator is grounded. The electrical-equivalent model for the resonator is as shown in Fig. 8 (d) but with a 180° phase change in the output current due to the in-phase motion of all the faces of the plate resonator.

The measurements are done with the MEMS resonator and a JFET (junction field-effect transistor) preamplifier in vacuum using a -50 -dBm desired signal (corresponding to a 50Ω source impedance) at the resonator input at the resonance frequency of $\bar{\omega}_0$ and considering two 0 -dBm interferers at $\omega_1 = \bar{\omega}_0 + \Delta\omega$ and $\omega_2 = \bar{\omega}_0 + 2\Delta\omega$. The simulations are done in Aplac® circuit simulator using harmonic balance [85]. As seen in Fig. 11, the infinite- Q limit of (28) becomes valid as soon as the interferers are outside the resonator passband. Also, as predicted by the theory, at the intermediate frequencies of $50 \text{ Hz} < |\Delta f| < 1 \text{ kHz}$ we observe that the SIR is much lower for interferers below the resonance ($\Delta\omega < 0$) than for interferers above the resonance ($\Delta\omega > 0$). This difference is at greatest when the interferer frequencies are close to the 3 -dB-passband edge of the resonator. Within the passband, the in-band approximation (29) becomes valid. The excellent agreement between the analytical, simulated and measured results

verifies the theory for weakly coupled ($R_m \gg \{R_{ac}, Z_L\}$) single-stage capacitive MEMS filters.

The previously reported experimental IM3 results [84] for $\Delta\omega \ll -\omega_0/Q$ are in good agreement with (28). For example, assuming that the spring constant of the clamped-clamped-beam resonator of [84] can be approximated by a point-force result [86], (28) and (16) give the same IIP3 voltage as reported in [84]. On the other hand, for $\Delta\omega > 0$ as well as for the interferers close to the passband edge, results of Publication II and (28) differ from the analytical result of [84].

2.4 Generalization of the IM3 Theory

With source and load impedances that are large enough to not be ignorable, a parallel-to-series impedance transformation is utilized as shown in Fig. 12 for a single-resonator MEMS filter. Here the load impedance is represented by a resistance R_L and capacitance C_L in parallel. Loading of the resonator due to the source and load impedances can now be taken into account by using a loaded dissipation and spring constant

$$\gamma' = \eta^2 (R_m + R'_S + R'_L) \quad (30 \text{ a})$$

$$k' = \eta^2 (1/C_m + 1/C'_S + 1/C'_L), \quad (30 \text{ b})$$

to find a loaded quality factor, $Q' \equiv \sqrt{k'm}/\gamma'$, and resonance frequency, $\omega' \equiv \sqrt{k'/m}$. The series-equivalent resistances and capacitances of Fig. 12 in (30 a) and (30 b) are (see, for example, [87])

$$R'_S = \frac{R_{ac}}{(R_{ac}\omega'C_0)^2 + 1} \quad (31 \text{ a})$$

$$C'_S = \frac{C_0 [(R_{ac}\omega'C_0)^2 + 1]}{(R_{ac}\omega'C_0)^2} \quad (31 \text{ b})$$

$$R'_L = \frac{R_L}{[R_L\omega'(C_0 + C_L)]^2 + 1} \quad (31 \text{ c})$$

$$C'_L = \frac{(C_0 + C_L) \{[R_L\omega'(C_0 + C_L)]^2 + 1\}}{[R_L\omega'(C_0 + C_L)]^2}. \quad (31 \text{ d})$$

In addition to using the loaded quality factor, Q' , the Thévenin-equivalent input voltage

$$u' = u \times \frac{1}{1 + j\omega'C_0R_{ac}} \quad (32)$$

must be used in order to be able to utilize the unloaded SIR and IIP3 results (28) and (29) for tightly-coupled filters.

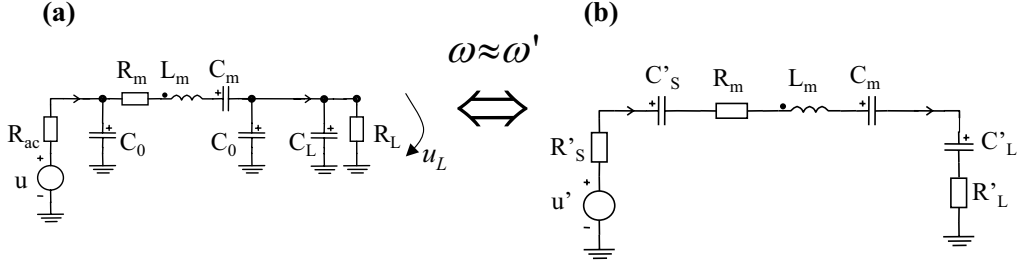


Figure 12: Parallel-to-series impedance transformation for a single-stage MEMS filter. For example, u and R_{ac} can model an antenna while C_L and R_L represent an LNA input.

For filter design, (28) and (29) can be further simplified by assuming that: i) the pass-band desired-signal frequency is much higher than the frequency separation to the interferers present in the filter input, ii) the bias voltage is much lower than the electromechanical pull-in voltage, and iii) mechanical spring nonlinearities can be ignored as much weaker than the capacitive transducer nonlinearities. With these assumptions we find from (28)

$$\text{SIR} = \frac{8 |\Delta\omega| \omega'}{5 \omega_e^2} \times \frac{V^2}{R'_S \Gamma_{\text{int}}} \sqrt{\frac{P_{\text{sig}}}{P_{\text{int}}^3}}. \quad (33)$$

The AC-source powers for the signal and interference are $P_{\text{sig}} = u_{\text{sig}}^2/(2R_{ac})$ and $P_{\text{int}} = u_{\text{int}}^2/(2R_{ac})$, respectively. When the interferers are inside the passband, we have from (29) and (16) generalizing to $\Gamma_{\text{int}} \neq 0$

$$\text{SIR}_{\text{IB}} = \frac{1}{\sqrt{(6p^3 + p/2)^2 + 9p^4}} \times \frac{V^2}{R'_S \Gamma_{\text{int}}} \sqrt{\frac{P_{\text{sig}}}{P_{\text{int}}^3}}, \quad (34)$$

where $p \equiv Q' \omega_e^2 / \omega'^2 = Q' k_e / k'$.

In Publication III, it is shown that as $\text{SIR}(\Delta\omega) \rightarrow \text{SIR}(-\Delta\omega)$ for out-of-band interferers with $|\Delta\omega| \rightarrow \infty$, (33) becomes valid. Furthermore, outside the passband the single-resonator result (28) is also valid for higher-order filters as well as for the tightly-coupled filters provided that the loaded quality factor and the Thévenin-equivalent input voltage of (32) are used as discussed above. Intuitively, this is to be expected as for the out-of-band interferer frequencies, the resonator impedances are high and the resonators are therefore only weakly coupled. Furthermore, as typically the capacitive nonlinearity is much stronger than the mechanical spring nonlinearities, the transducers effectively set the IIP3. Moreover, except close to the passband edge, the force nonlinearity of the first transducer is the dominant source of intermodulation (Publication II).

For in-band frequencies, the IIP3 for higher-order filters depends on the chosen desired-user frequency within the passband. However, the single-stage approximation is still a good order-of-magnitude estimation (Publication III).

2.5 Design Principles of MEMS Filters

In what follows, we derive design criteria for the resonator dimensions, transducer gap, Q value and bias voltage from specified in-band and out-of-band filter attenuation and maximum distortion. The criteria yield a systematic procedure to design MEMS filters for communication systems. We focus on receiver (RX) applications.

Out-of-band attenuation: For minimum performance, the filter should suppress the interferers situated outside the systems RX band to the same level as the strongest interferers within the RX band. If this is achieved, the linearity requirement for the LNA and mixer are set by the in-band interferers that normally are not affected by band-select filtering. Denoting the minimum attenuation at frequency ω with respect to the desired-signal frequency, ω' , as A_{\min} , the minimum required loaded in-circuit quality factor can be found. For the single-stage MEMS filter, this leads to

$$Q' \geq \frac{\sqrt{A_{\min}^2 - (\omega/\omega')^2}}{|1 - (\omega/\omega')^2|} \equiv Q'_{\min}. \quad (35)$$

Increasing the filter order makes the stop-band response a steeper function of frequency and thus a lower quality factor for the resonators is sufficient at the cost of higher insertion loss.

Out-of-Band Intermodulation: The weakest signal, with power P_{sig} , to be detected in the presence of interferers, having powers P_{int} at $\omega' + \Delta\omega$ and $\omega' + 2\Delta\omega$, leads to requirements for intermodulation performance. Typically, this is specified with the minimum SIR (SIR_{\min}) that the filter needs to satisfy in its output in order to meet the target for the overall systems carrier-to-interference (C/I) ratio. Requiring the SIR to be greater than or equal to the minimum SIR_{\min} gives from (33)

$$d^3 + (\epsilon_0 A \omega' R_{\text{ac}})^2 d \geq \frac{5}{8} R_{\text{ac}} \Gamma_{\text{int}} \text{SIR}_{\min} \frac{\epsilon_0 A}{m |\Delta\omega| \omega'} \sqrt{\frac{P_{\text{int}}^3}{P_{\text{sig}}}}, \quad (36)$$

which can also be used for higher-order filters as discussed above. Thus in order to meet the performance requirements given as SIR_{\min} , there is a minimum value for the gap.

In-Band Loss: The passband voltage gain, $G_V \equiv 2u_L/u$, is easily found using the circuits of Fig. 12 and assuming n identical filter stages. Requiring that the passband voltage gain is larger than a specified minimum acceptable value, G_{\min} ,

a lower limit for QV^2 is found as

$$QV^2 \geq \frac{nd^4\sqrt{km}}{(\epsilon_0 A)^2 \left\{ \frac{2}{\omega' C'_L G_{\min}} \frac{|1 + j\omega' C'_L R'_L|}{|1 + j\omega' C'_0 R_{\text{ac}}|} - R'_S - R'_L \right\}}. \quad (37)$$

Thus, after choosing the gap, d , the unloaded quality factor, Q , and the bias voltage, V , need to be chosen to meet the insertion loss specifications. As the unloaded quality factor is usually determined by material properties, effectively this gives a requirement for the bias voltage. It is to be noted that with a dominantly capacitive termination ($|1/\omega' C'_L| \gg R'_L$) it is possible to obtain voltage gain as the filter acts as an RLC impedance transformer.

In-Band Intermodulation: The in-band intermodulation is estimated from (34) by considering the i) signal self distortion and ii) in-band interferers. However, typically the out-of-band interferers give more stringent linearity requirements. Therefore, after choosing the filter parameters, it is usually sufficient to check that the filter meets the in-band specifications. If these are not met, then the filter gap should be increased and the design adjusted accordingly.

2.6 Design Example

In the following, the usage of the above results is illustrated by a single-stage MEMS front-end filter design for $f_0 = 1$ GHz with requirements of GSM 900 mobile device. The simplified specifications are shown in Table 2. These should be considered as exemplary performance requirements and a realistic system design may set a more or less stringent goals.

Table 2: Simplified RX front-end filter requirements for GSM 900 [83].

Specification		Comment
SIR_{\min}	12 dB	$\rightarrow (36)$
G_{\min}	-3 dB	$\rightarrow (37)$
$A_{\min}(f - f_0 = 10 \text{ MHz})$	23 dB	$\rightarrow (35)$
to be met with:		
P_{sig}	-99 dBm	Signal
$P_{\text{int}}(\Delta f = 0 \text{ Hz})$	-49 dBm	In-band interferer
$P_{\text{int}}(\Delta f = 600 \text{ kHz})$	-43 dBm	In-band blocker
$P_{\text{int}}(\Delta f = 10 \text{ MHz})$	0 dBm	Out-of-band blocker

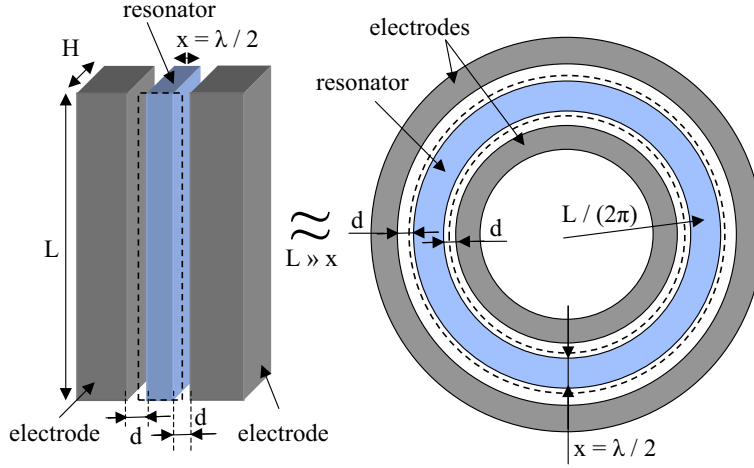


Figure 13: Test geometry for resonator design showing the resonator surrounded by the electrodes. The dotted line indicates the vibration mode shape in extended state.

Resonator geometry: Several structures have been utilized in MEMS microresonators such as bending and stretching beams (see Fig. 3) as well as bulk-acoustic circular [39] or square [8] plates or ring resonators [37]. In order to reach UHF frequencies, micromechanical bending-mode resonators are unpractical since the fundamental frequencies are at HF range (< 30 MHz) and coupling to harmonics of high order is difficult. Bulk-acoustic circular or square plate resonators can have the first vibration mode at VHF range and the second or third harmonic already at ~ 1 GHz [39]. Alternatively, one can utilize the fundamental bulk-acoustic mode of a thin bar or ring for which a very high quality factor is reported in [37]. Above 1 GHz, however, the thickness of the bar becomes only few microns and can easily be limited by fabrication accuracy. As in Publication III, we consider here the bar and ring geometries, shown in Fig. 13, to illustrate the usage of the design equations developed in Sec. 2.5. Other resonator structures can be treated in a similar fashion.

The resonating dimension of the bar in Fig. 13 is $x = \lambda/2 = v/(2f_0) \approx 4\mu\text{m}$ for $f_0 = 1$ GHz. Here $v = \sqrt{Y/\rho}$ is the bulk-acoustic wave velocity with $\rho = 2330$ kg/m³ the density and $Y = 168$ GPa the Young's modulus of silicon. The bar can also approximate the ring geometry of [37], shown on the right-hand side of Fig. 13, when the ring radius $L/(2\pi)$ is much larger than the ring width x . The capacitive transducers at both sides of the resonator have an area of $A = HL$ and a rest capacitance of $C_0 = \epsilon_0 HL/d$. The mass and spring coefficient are now [34]

$$m = \rho LxH/2 \quad (38\text{ a})$$

$$k = \pi^2 Y L H / (2x). \quad (38\text{ b})$$

We consider a typical thickness of the SOI device layer of $H = 10\mu\text{m}$ after which the resonator length L is varied to find a good geometry. For square plate, instead

of (38 a) and (38 b), one would use $m_{\text{sp}} = \rho H L^2$ and $k_{\text{sp}} = \pi^2 Y_{2\text{D}} H$, where $Y_{2\text{D}}$ is the effective elastic modulus for the extending plate [8].

Minimum quality factor: From the minimum requirements for the interference attenuation in Table 2, one obtains with (35) a value of $Q'_{\text{min}} = 700$ for the minimum loaded quality factor. For channel-select filtering in GSM 900, the passband is 200 kHz corresponding to a much higher in-circuit quality factor of $Q' = 5000$, which would also be enough for $A_{\text{min}} = 40$ dB at 10 MHz off the passband in (35) as is typically satisfied by commercial FBAR filters. As higher Q values enable lower bias voltages for the same insertion loss (37), we set the unloaded quality factor to $Q = 2000$, which could be feasible [37], resulting in an unloaded 3-dB bandwidth of 500 kHz.

Minimum gap: The intermodulation requirements set the minimum value for the gap. In Publication III, the filter design is considered with two 0-dBm out-of-band blockers of Table 2 at 10 MHz and 20 MHz off the passband edge. Consequently, the gap minimum is found to be in between 10 nm and 100 nm depending on parameter values. Here we consider only one 0-dBm blocker of Table 2 together with an in-band interferer at $f_0 + 5$ MHz with a power of -49 dBm. In this case (36) yields the lower limit for the gap to be as low as ~ 1 nm. As the gap width is more likely to be limited by the fabrication technology, we consider $d \in \{10, 30, 90\}$ nm in what follows.

Load impedance: In Publication III both resistive and capacitive filter terminations are analyzed. It is shown, in particular, that the requirements of low-enough bias voltage, good linearity and low insertion loss are difficult to be met for battery-powered devices if the conventional resistive 50- Ω source and load termination is to be used. As a capacitive termination enables voltage gain in the filter and thus a lower insertion loss than for a resistive load with the same bias voltage, we consider here only a capacitive termination with $R_L = 1$ M Ω and $C_L = 0.1$ pF. Such an environment for the filter could be realized in an integrated RX architecture where the filter output is directly connected to a capacitive FET LNA (low-noise amplifier) load (C_L and R_L in Fig. 12) while the filter input is fed from a resistive source such as an antenna (u and R_{ac} in Fig. 12).

Bias Voltage: After setting values for the gap, d , resonator length, L , and the AC source impedance, R_{ac} , the minimum bias voltage can be solved from (37) as shown in Fig. 14, where the voltage is drawn as a function of the resonator length for different values of the transducer gap and the source resistance. For low-voltage operation, the gap has to be well below 100 nm. For example, the design marked with the circle in Fig. 14, for which $d = 30$ nm, $R_{\text{ac}} = 50$ Ω and $L = 200$ μm , needs a bias of 12 V. Other parameters for this filter solution are given in Table 3.

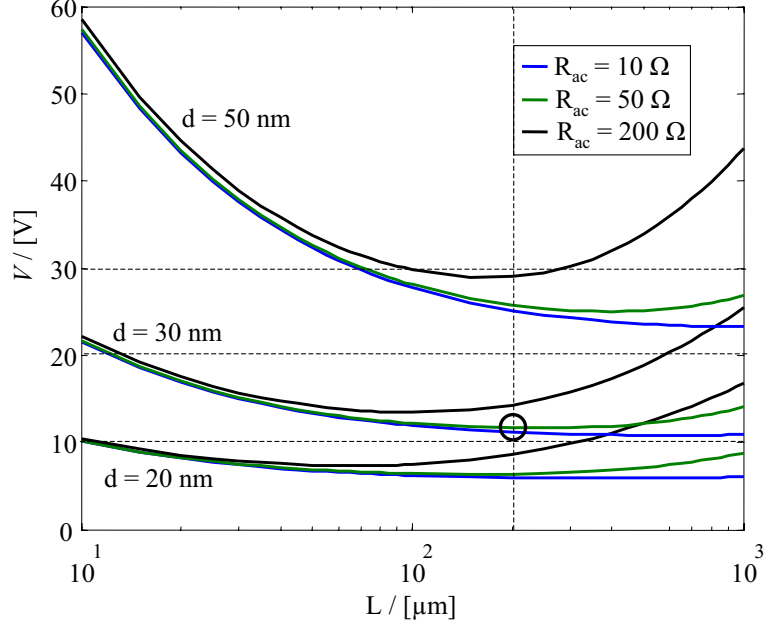


Figure 14: Minimum bias voltage meeting the insertion-loss specification (37).

Table 3: Exemplary filter design that is marked with a circle in Fig. 14.

f_0	[GHz]	1	R_m	[Ω]	560	Q		2000
H	[μm]	10	R_L	[$M\Omega$]	1	Q'		1840
L	[μm]	200	C_L	[pF]	0.1	V_{pi} (12 a)	[V]	420
k	[MN/m]	390	R_{ac}	[Ω]	50	G_V	[dB]	-2.5
m	[fg]	9.9	V	[V]	12	SIR (33)	[dB]	99
d	[nm]	30	C_0	[fF]	590	SIR _{IB} (34)	[dB]	110

3 Acoustic Transmission Lines

Acoustic transmission lines have been utilized in several applications. For example, in wireless passive SAW RFID tags and sensors, the transmitted data is coded into a multitude of reflections of a SAW pulse that is generated (in response to a received radio pulse) and detected by an antenna connected to a SAW chip [88]. In these applications, long acoustic delays and short transmission distances guard against interference from multipath radio propagation. In radar systems, delay lines are used, for example, to create a delayed replica of the transmit signal to correlate it with the received signal reflected from the target [89], to compensate for phase errors in FMCW radars [90], or to simulate a target. In delay-line oscillators, long delay stabilizes the frequency and suppresses off-carrier phase noise [91–93]. Delay-line based information processing has been applied, for example, to implement convolution [94]. Analog delays are also proposed for novel ultra-wideband receivers [95]. In video systems, delay lines are used, for example, in event recorders and action replay. In this work a capacitively-coupled bulk-acoustic micro-sized transmission line is analyzed and a new MEMS delay-line structure for long time delays, consisting of a chain of coupled resonators, is introduced.

3.1 Bulk-Wave Waveguides

An acoustic transmission line for high frequencies is obtained when the mechanical resonator of Fig. 8 (c) is replaced with an elastic continuous medium obeying the wave equation as shown in Fig. 15. Here longitudinal bulk-wave propagation is utilized for signal transmission in an electrostatically-coupled micro-sized silicon rod of the kind analyzed in detail in Publication IV. In Fig. 15, the wave equation for the mechanical displacement y along the rod is

$$\frac{\partial^2 y(x, t)}{\partial t^2} = c^2 \frac{\partial^2 y(x, t)}{\partial x^2}, \quad t \geq 0, \quad x \in [0, \Delta x], \quad (39)$$

where $c^2 = Y/\rho$ with Y being the Young's modulus and ρ the density of the rod material. The boundary conditions are

$$\left. \frac{\partial y(x, t)}{\partial x} \right|_{x=0} = \frac{F_1}{AY}, \quad \left. \frac{\partial y(x, t)}{\partial x} \right|_{x=\Delta x} = \frac{F_2}{AY}, \quad (40)$$

where F_1 and F_2 are the electrostatic forces of (23 a) and (23 b) of the input and output transducers, respectively.

Solving the wave equation as is done in Publication IV, allows one to identify the input impedance in Fig. 15 as $Z = Z_0 || Z_{\text{em}}$, where Z_{em} for small k_e obeys the standard transmission-line equation [96]

$$Z_{\text{em}} = Z_c \frac{Z_T + Z_c \tanh(j\beta\Delta x)}{Z_c + Z_T \tanh(j\beta\Delta x)}, \quad (41)$$

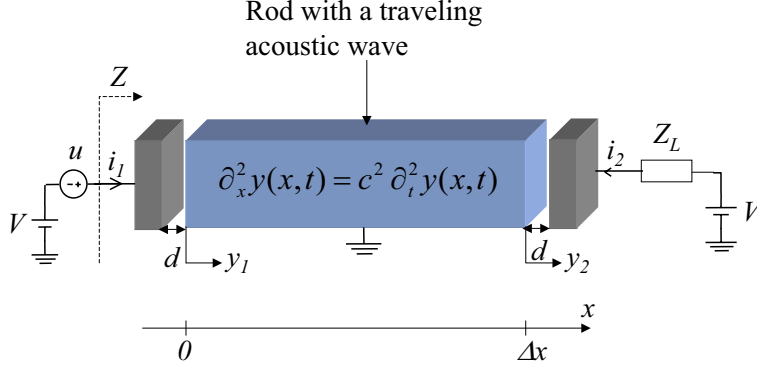


Figure 15: Schematic representation of a setup where an electric signal is transmitted through a micromechanical rod as an acoustic plane longitudinal wave.

where $\beta \equiv \omega/c$, $Z_c \equiv AY/(c\eta^2)$ and $Z_T \equiv Z_0 || Z_L$. The mechanical losses can be included in (41) by substituting $j\beta$ with $j\beta + \alpha$ where α is the attenuation coefficient [96, 97]. For zero reflection at the output, one needs $Z_T = Z_c$, which gives with (41)

$$Z_{\text{em}} = Z_c = \frac{AY}{c\eta^2} = \frac{A\sqrt{\rho Y}}{\eta^2} = \frac{d^4 \sqrt{\rho Y}}{A(\epsilon_0 V)^2}. \quad (42)$$

Here $A\sqrt{\rho Y}$ is the mechanical characteristic impedance of the rod [98]. The corresponding matched load impedance is $Z_L = (Z_c || Z_0^*)$. Thus Z_c can be seen as an electrical characteristic impedance of the acoustic waveguide.

For practical realisation of the MEMS waveguide, impedance matching is a challenge. This is because the weakness of the capacitive coupling makes the characteristic electrical impedance, Z_c , in (42) extremely high. As (42) shows, Z_c can be made smaller by having a smaller gap, d , softer or sparser rod material (smaller Y or ρ), a larger area, A , higher-permittivity material in the gap or a higher bias voltage, V . On the other hand, the maximum displacement of the end of the rod is limited by pull-in. For example, for a silicon rod with $Y = 168$ GPa, $\rho = 2330$ kg/m³, $A = 10 \times 100$ (μm)², $d = 100$ nm and $V = 100$ V, one finds $Z_c = 2.5$ M Ω while the lower limit for Z_c , given by pull-in, is 2.1 M Ω (see Publication IV) for a 1 mm long rod.

3.2 Resonator Chains

A capacitively-coupled spring-mass-chain waveguide of Publications V and VI, shown in Fig. 16 without dissipation, is composed of elementary resonators that can be modelled with two identical moving masses, m , that are coupled with a spring of strength k_c and anchored to a stationary support with springs of strength k_a . Except for the ends, the chain is periodic with period a . The waveguide can be seen as a high-order bandpass filter [15, 16] with identical stages. Using a

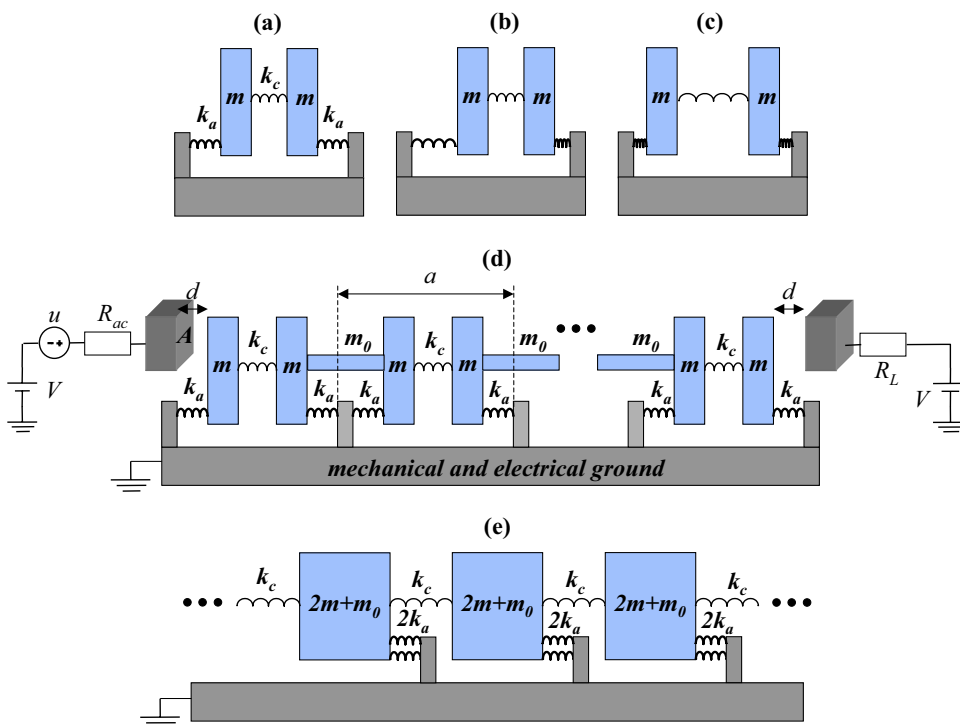


Figure 16: (a) An elementary two-mode resonator with (b) symmetric and (c) anti-symmetric eigenmodes. (d) Delay line consisting of capacitive input (left) and output (right) transducers with gap d and a chain of coupled resonators. Except for the ends of the chain, the waveguide can be modelled as shown in (e). Losses are not indicated.

weak inter-stage coupling spring, much lower characteristic impedances can be obtained than for the solid-rod waveguide of Sec. 3.1. However, not as high signal frequencies can be used than with bulk-wave propagation. In what follows, damping is not considered in the analytical work but is included in the numerical simulations.

The elementary resonator of Fig. 16 has two fundamental modes of vibration with resonance frequencies

$$\omega_s = \sqrt{\frac{k_a}{m}} \quad (43 \text{ a})$$

$$\omega_a = \sqrt{\frac{2k_c + k_a}{m}}. \quad (43 \text{ b})$$

In the symmetric mode with resonance frequency ω_s (43 a), the masses move in phase while in the antisymmetric mode with frequency ω_a (43 b), there is a 180° phase difference between the mass motions. A useful parameter is the ratio of the strength of the anchoring spring, k_a , to that of the coupling spring, k_c , determined as $K \equiv k_a/k_c = 2/[(\omega_a/\omega_s)^2 - 1]$. For a particular resonator

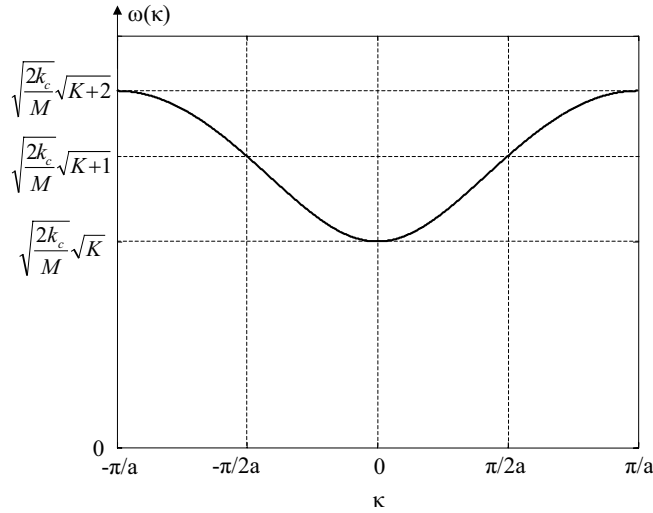


Figure 17: Dispersion relation for the anchored spring-mass chain of Fig. 16.

geometry, the ratio of the resonance frequencies is obtained, for example, from FEM eigenmode analysis or from measurements.

A periodic chain of coupled resonators can vibrate and carry signals at frequencies consistent with the dispersion relation, $\omega(\kappa)$, that gives the frequency, ω , as a function of the wave vector, $\kappa \equiv 2\pi/\lambda$, where λ is the wavelength. For the anchored chain of Fig. 16, the dispersion relation is found as a generalization of the familiar text-book result for periodic unanchored (free) chains [99]. One obtains for the anchored chain

$$\omega(\kappa) = \sqrt{\frac{2k_c}{M}} \sqrt{1 - \cos(\kappa a) + K}, \quad (44)$$

where $M \equiv 2m + m_0$ is the total coupled-resonator mass, a is the period of the chain and the wave vector, $\kappa \in [-\pi/a, \pi/a]$, is restricted to the first Brillouin zone [99]. The dispersion relation (44) is illustrated in Fig. 17. As opposed to the low-pass character of free chains, the nonzero k_a forbids zero-frequency oscillations and results in passband response.

Group velocity for signal propagation along the chain is found from (44) as $v_g = \partial\omega/\partial\kappa$, and it is seen to differ from the phase velocity $v_{ph} = \omega/\kappa$. For the center frequency $\omega_0 = 2\pi f_0$ and bandwidth $\Delta\omega = 2\pi\Delta f$ of the line one finds

$$\omega_0 = \omega\left(\frac{\pi}{2a}\right) = \sqrt{\frac{2k_c}{M}} \sqrt{K+1} \quad (45 \text{ a})$$

$$\Delta\omega = \omega\left(\frac{\pi}{a}\right) - \omega(0) = \sqrt{\frac{2k_c}{M}} \left(\sqrt{K+2} - \sqrt{K} \right). \quad (45 \text{ b})$$

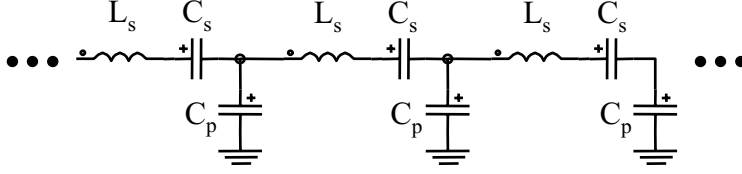


Figure 18: Electrical-equivalent model for the spring-mass-chain transmission line in Fig. 16 for center-band operation.

At the center of the passband, one obtains for the phase and group velocities

$$v_{\text{ph}}^0 \equiv \frac{\omega}{\kappa} \Big|_{\omega_0} = \frac{2a}{\pi} \sqrt{\frac{2k_c}{M}} \sqrt{K+1} \quad (46 \text{ a})$$

$$v_g^0 \equiv \frac{\partial \omega}{\partial \kappa} \Big|_{\omega_0} = \frac{a}{2} \sqrt{\frac{2k_c}{M}} \frac{1}{\sqrt{K+1}} \quad (46 \text{ b})$$

illustrating clearly the dispersive character of the spring-mass chain.

Solving for the propagation constant κa in (44) and expanding its square as a power series with respect to ω^2 around the passband center frequency, allows one to identify the elements of the electrical-equivalent circuit of the transmission line as depicted in Fig. 18 (see, for example, [100]), where

$$L_s = \frac{M}{\eta^2} \quad (47 \text{ a})$$

$$C_s = \frac{\pi \eta^2}{2k_c [\pi(1+K) - (\pi/2)^2]} \quad (47 \text{ b})$$

$$C_p = \frac{\pi \eta^2}{2k_c} . \quad (47 \text{ c})$$

Consequently, one finds for the characteristic impedance of the line

$$Z_c = \sqrt{\frac{Z_s}{Y_p}} = \frac{\sqrt{k_c M}}{\eta^2 \sqrt{2(K+1)}}, \quad (48)$$

where $Z_s = j\omega L_s + 1/(j\omega C_s)$ is the series impedance and $Y_p = j\omega C_p$ is the shunt admittance in Fig. 18.

Increasing the strength of the anchoring spring, k_a , with respect to that of the coupling spring, k_c , increases the center frequency (45 a) and phase velocity (46 a) while decreasing the bandwidth (45 b), group velocity (46 b) and the characteristic impedance (48) that, typically, is much higher than $50 \, \Omega$ with electrostatic coupling. Furthermore, for higher K , the variation of the group velocity as a function of frequency at the band center is reduced. For good signal coupling and long delays, it is thus desirable to have K as high as possible.

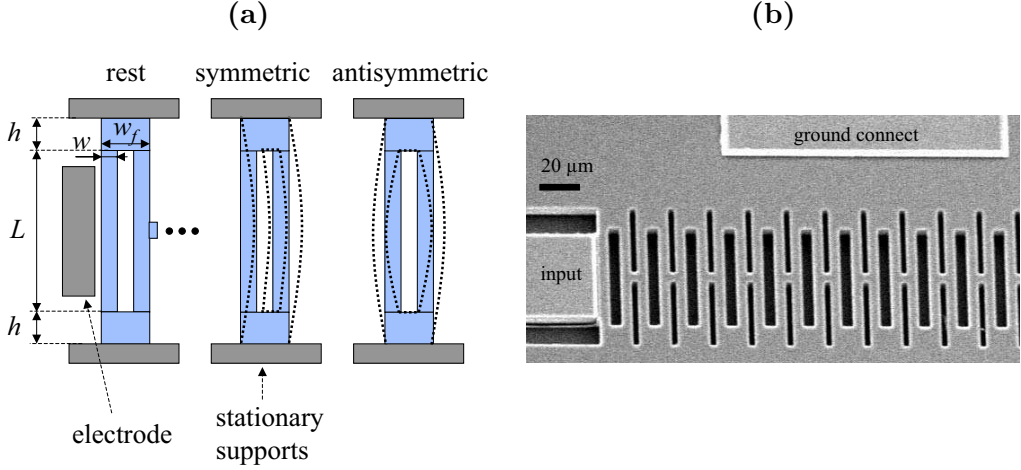


Figure 19: (a) Schematic of a resonator-chain design with an elementary tuning-fork resonator having symmetric and antisymmetric eigenmodes. Here, in particular, $w = 5 \mu\text{m}$, $w_f = 15 \mu\text{m}$ and $L = 50 \mu\text{m}$. (b) SEM micrograph of a fabricated structure.

3.2.1 Measurements of Test Structures

The theory for the spring-mass-chain transmission lines is validated in Publication VI with measurements of fabricated narrow-gap waveguides of various lengths having different resonator structures. Figure 19 illustrates one of the designs that is discussed in detail in Publication VI. Figure 20 shows a measurement result and an Aplac® simulation fit for the response of the waveguide of Fig. 19 composed of 80 elementary two-mode resonators in series with a period of $a = 17.5 \mu\text{m}$. The numerical result that reasonably well fits the measurement is obtained by varying the parameters of the device. In particular, one finds for the quality factor of the elementary resonators $Q = 8000$, spring-constant ratio $K = 8.5$ and gap $d = 230 \text{ nm}$ corresponding to a group velocity of $v_g^0 = 70 \text{ m/s}$ and a characteristic impedance of $Z_c = 6 \text{ M}\Omega$. The passband ripple and high loss are due to impedance mismatch at the input and output of the waveguide. Matched termination would require the source and load impedances to equal the characteristic impedance. However, practical matching also requires the transducer (Z_0), bonding-pad (Z_{pad}) and parasitic feed-through (Z_{thr}) impedances to be smaller than Z_c .

3.2.2 Minimizing the Characteristic Impedance

As shown above, the MEMS resonator-chain delay lines enable record high acoustic time delays in a given physical size. However, to facilitate matched source and load termination for the line and to avoid using a differential readout, a much lower characteristic impedance, well below the pad, feed-through and transducer impedances, is needed than what was obtained above. As shown by (48) this can

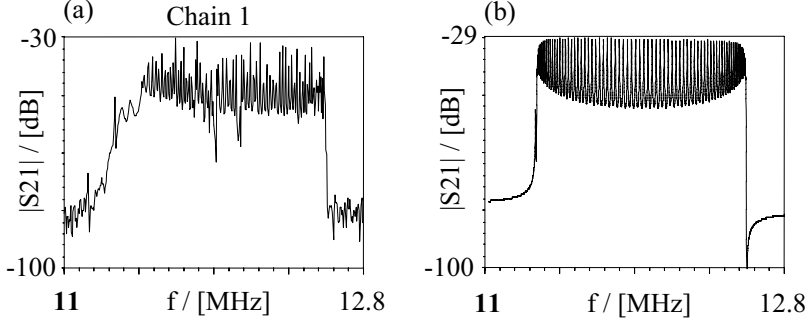


Figure 20: Measured (a) and simulated (b) response of the transmission line of Fig. 19 with 80 resonators.

be achieved by enhancing the coupling, η , and by strengthening the anchoring spring, k_a , with respect to the coupling spring, k_c , (larger K). Reducing the anchoring height, h , in Fig. 19 to $5\ \mu\text{m}$, doubling the beam separation ($w_f \rightarrow 20\ \mu\text{m}$) and taking the narrowing of the structures in fabrication into account in the design, a much higher spring-constant ratio of $K = 74$ is expected. For good signal coupling, it is also important to design the first and last resonator in the chain to compensate for the electrical spring softening as well as for the stiffening of the first and last beams due to the capacitive coupling occurring over the transducer area as opposed to the point-force inter-resonator coupling along the chain. If, in addition, the transducer gap is reduced to $d = 100\ \text{nm}$, a delay line with a period of $a = 22.5\ \mu\text{m}$, estimated characteristic impedance of $Z_c = 22\ \text{k}\Omega$, bandwidth of $\Delta f = 185\ \text{kHz}$ and group velocity of $v_g^0 = 13\ \text{m/s}$ can be obtained with a bias voltage of $30\ \text{V}$ ($V_{\text{pi}} = 38\ \text{V}$ (12 a)).

Figure 21 shows the simulated response and group delay for a low-impedance chain of 80 resonators with reduced pad ($C_{\text{pad}} = 91\ \text{fF} \Rightarrow Z_{\text{pad}} = 127\ \text{k}\Omega$) and feed-through capacitances ($C_{\text{thr}} = 8\ \text{fF} \Rightarrow Z_{\text{thr}} = 1.3\ \text{M}\Omega$) that are likely obtainable with wafer-level vacuum packaging and IC integration. The transducer capacitance is $C_0 = 37\ \text{fF}$ corresponding to $Z_0 = 308\ \text{k}\Omega$. Consequently, the characteristic impedance of the transmission line is much lower than Z_{pad} , Z_{thr} and Z_0 as required by good signal coupling. To have a flat group delay at the band center, resistive source and load termination to $R_L = 14\ \text{k}\Omega$ is used that is somewhat lower than the estimated characteristic impedance of $22\ \text{k}\Omega$. Higher pad and feed-through capacitances result in passband ripple and increased insertion loss if the characteristic impedance is not simultaneously further lowered.

Figure 22 illustrates a low-power transponder terminal, communicating with on-off keying, for example, in a low-datarate sensor application. Here, the reader sends an RF pulse to the sensor in which the pulse is either retransmitted back to the reader (bit 1) or shunted to ground (bit 0). Utilizing the above low-impedance design, for a datarate of $80\ \text{kb/s}$, one could use a delay line of $12\ \mu\text{s}$ time delay (chain of 7 resonators) and a time pulse of $\Delta T_{\text{pulse}} = 10\ \mu\text{s}$.

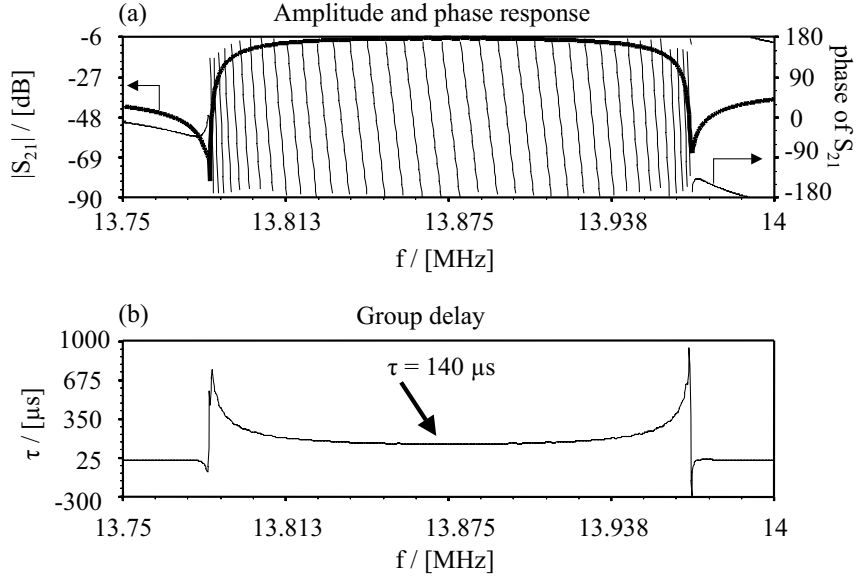


Figure 21: Simulated response (a) and group delay (b) for the low-impedance delay line with $14 \text{ k}\Omega$ source and load impedance. In (a) the thick line is for the amplitude and the thin line for the phase of S_{21} .

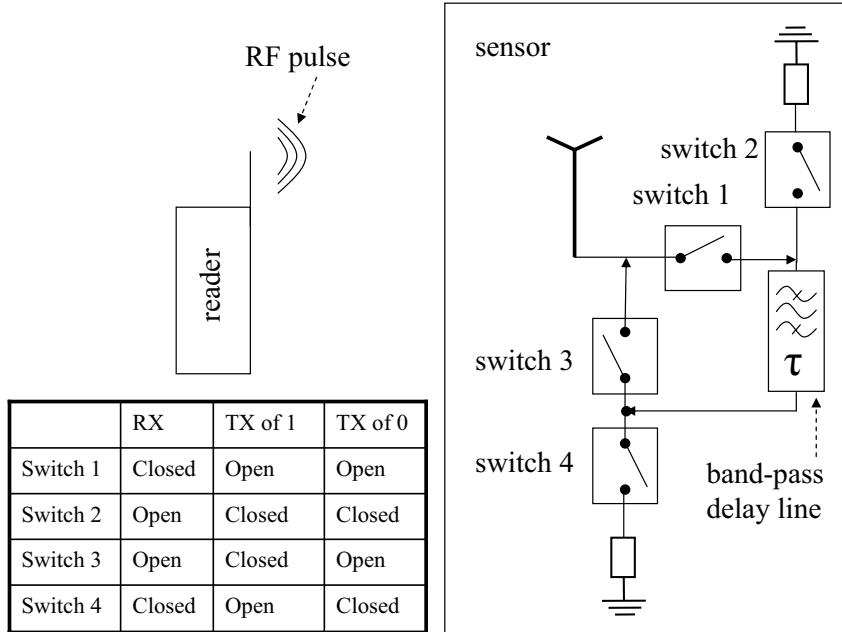


Figure 22: Schematic of a simple delay-line transponder for low-power low-datarate communication in sensor applications. The switch states in RX and TX are indicated in the table. Switch 2 is needed to have a proper source and load termination for the delay line at all times.

4 Discussion on Frequency Scaling

It is of interest to consider the scaling of the device properties as a function of frequency. In single-crystal bulk silicon, the attenuation factor at $f = 1$ GHz for longitudinal waves in the cube-edge direction is $\alpha = 1000 \text{ dB/m}/(20 \log_{10} e) \sim f^2$ [97]. This results in the scaling of the acoustic quality factor as $Q = \pi f / (v\alpha) \sim f^{-1}$, where v is the wave velocity [97]. For $f = 1$ GHz, one obtains $Q = 3200$ which, however, is somewhat exceeded by the state-of-the-art silicon MEMS resonators [37]. Let us now consider three different bulk-acoustic (BAW) resonators in the circuit of Fig. 12 with a capacitive load: i) the 1D ring resonator of Fig. 13 with only the width x scaling as $x \sim f^{-1}$, ii) the 2D plate of [8] and Fig. 3 (c) with the lateral dimensions but not the SOI thickness scaling as $\sim f^{-1}$, and iii) a 3D resonator for which all the dimensions scale as $\sim f^{-1}$ as considered in [32]. We further assume that i) the bias and AC voltages, transducer gap, R_{ac} , $R_L \gg 1/(\omega C_L)$, and C_L do not scale with the frequency, ii) the transducer impedance Z_0 is much higher than the source impedance R_{ac} , and iii) the bias voltage is much lower than the pull-in voltage. With these assumptions, we find the scaling exponents of relevant resonator properties that are given in Table 4. Here the same SIR scaling is obtained both for (33) outside the pass-band with $\Delta\omega \sim \omega/Q$ and for (34) within the band. Although scaling of the motional impedance depends on the chosen geometry, the nonlinearity-limited critical amplitude, $x_{0,c}$, [32], pull-in voltage, SIR and voltage gain have more universal exponents. It is interesting to note that increasing the frequency enhances SIR but degrades the voltage gain.

Table 4: Frequency scaling exponents of resonator properties.

symbol	k	m	Q	C_0	η	R_m	$x_{0,c}$	V_{pi}	SIR	G_V
1D ring	1	-1	-1	0	0	1	-1/2	1/2	2	-2
2D plate	0	-2	-1	-1	-1	2	-1/2	1/2	2	-2
3D	-1	-3	-1	-2	-2	3	-1/2	1/2	2	-2

For the spring-mass-chain delay lines, the frequency scaling can be estimated based on the clamped-clamped flexural-beam resonator for which $m \sim wHL$ and $k \sim H(w/L)^3$ [32]. For $w \sim L \sim f^{-1}$, $H \sim f^0$ and $w \sim L \sim H \sim f^{-1}$, the resonator scaling is the same as for the 2D-plate resonator and the 3D resonator in Table 4, respectively. Assuming that both the anchoring and the coupling springs of the tuning forks scale as k (keeping the spring-constant ratio K constant), the group velocity is found not to scale with frequency. The characteristic impedance, on the other hand, scales as $Z_c \sim f$ for $H \sim f^0$ while for $H \sim f^{-1}$ we have $Z_c \sim f^2$. Thus for higher frequencies, the impedance matching becomes increasingly challenging, especially if the device-layer thickness needs to be reduced.

5 Conclusions

Microelectromechanical systems are beginning to provide a competitive alternative for many components used in radio architectures of commercial battery-powered communication devices. Several start-up companies are commercializing RF MEMS switches, filters and oscillators with the MEMS switch already being sold by a few companies such as TeraVista. The MEMS switch has a better contact resistance than, for example, CMOS or GaAs switches but the reliability still needs to be improved and the voltage levels of capacitively-actuated switches need to be lowered. The MEMS oscillator offers clear size and integration advantages compared to conventional quartz oscillators. They are being commercialized, for example, by Discera and SiTime as well as by VTT and VTI Technologies. Unlike a quartz oscillator, however, the MEMS oscillator requires external temperature compensation. Piezoelectrically-actuated FBAR filters, that often are also considered as MEMS devices, have already replaced SAW filters in some cell phones. Focusing on the research questions stated in Sec. 1.6, this thesis has created new scientific knowledge that is vital for RF MEMS filter design and introduced a new kind of MEMS delay line that can be used, for example, in time-delay radios.

Filter Distortion: In this thesis, intermodulation properties of capacitively-coupled bandpass MEMS filters were analytically solved in closed form and the trade-off between linearity and insertion loss was quantified. The theoretical results were verified in circuit simulations as well as in measurements. Also mechanical nonlinearities were included although, typically for good coupling, the capacitive nonlinearity is the dominant source of intermodulation. The theory was first formulated for weakly-coupled single-stage filters and then generalized to strong coupling (low motional resistance and low insertion loss) and to higher-order filters. What was not taken into account was the fact that for strong interferers present within the passband, Duffing effect can result in signal compression that limits the filter performance.

The obtained formulas are more generally applicable than the previously published results. In particular, the results of this thesis showed good accuracy also close to the passband edge and revealed the unsymmetry in intermodulation between positive and negative frequency separations of the interferers from the passband. In [57], an analytical result for intermodulation in a thermally actuated MEMS resonator is given that is in exact agreement with (28) if all terms other than the one originating from the third-order mechanical nonlinearity in the denominator are ignored. However, [57] uses an interferometric readout, which is not suitable for commercial communication applications, and does not consider insertion loss that is of importance in filter design.

After the analysis, a systematic procedure to design MEMS filters was formulated. The conventional resistive 50- Ω source and load termination was shown to typically result in a high insertion loss if good linearity is required with low-voltage

operation. Consequently, it was found desirable to utilize the high resonator Q for voltage gain that is enabled by capacitive load termination at the filter output. This is possible in integrated receiver architectures, where $50\ \Omega$ transmission lines are not needed between the antenna and the filter and between the filter and the LNA. With such an approach, MEMS filters could be used to construct a receiver front-end having a bank of narrow-band (ultimately channel-select) filters with different passbands to cover all the RX channels as suggested in [15]. Taking also the noise properties of MEMS resonators [79] into account in the filter design as well as practical demonstration of the optimized filters are left for future work.

Using dielectric media other than air/vacuum for the electrode gap has potential in lowering the electrical impedance and thus alleviating the need for a very narrow gap [14]. The analysis procedure derived in this thesis can be directly applied for such devices as long as an appropriate value for permittivity is used.

Delay Lines: Usage of electrostatically-actuated longitudinal waves in a silicon rod for signal transmission was analyzed in detail and challenges due to high impedance levels were quantified. For HF frequencies, a MEMS resonator-chain structure with record slow signal propagation was presented enabling miniaturization of time-delay components. The properties of the delay line were theoretically analyzed and the theory was verified in measurements with fabricated devices consisting of up to 80 series-connected MEMS resonators. The fabricated delay lines had still too high characteristic impedances for practical applications, but careful design can result in impedance levels of few kilohms that can be acceptable in integrated solutions with properly-designed impedance transformers. To reach higher frequencies, the lateral resonator dimensions have to be scaled down which, however, weakens the capacitive coupling (increases the line impedance) unless the reduced transducer area is compensated for by a smaller gap, thicker SOI device layer or a higher bias voltage. In addition to a group velocity that is much lower than that for other acoustic delay lines (SAW or BAW), the MEMS line is characterized by a narrow-band response. This can be utilized in applications that would otherwise require a separate bandpass filter as in wireless transponder radios of sensors for which a possible structure was suggested in Fig. 22. Compared to SAW devices, MEMS can dramatically reduce the size of the radio unit. Demonstration of such a transponder is left for future work.

In the fabrication of capacitive MEMS filters and delay lines, several challenges remain: i) The gap should be reduced to well below 100 nm to enable low-enough bias voltages. High-permittivity dielectrics can provide an alternative approach to better coupling. ii) The dimensional tolerances of the devices, manufactured with lithography, are poor leading to wide variations in the center frequency. iii) The parasitic feed through-capacitance may limit the filtering performance and a differential readout may be required. If these challenges are met, MEMS filters and transmission lines can have a large economic potential.

References

- [1] Ari T Alastalo, Mika Koskenvuori, Heikki Seppä, and James Dekker, “A Micromechanical Resonating RF Mixer,” in *34th European Microwave Conference*, 2004, pp. 1297–1300.
- [2] Ari Alastalo, Jukka Kyynäräinen, Heikki Seppä, Anu Kärkkäinen, Nadine Pesonen, Manu Lahdes, Tauno Vähä-Heikkilä, Panu Pekko, and James Dekker, “Wideband microwave power sensor based on MEMS technology,” in *Conference on Precision Electromagnetic Measurements (CPEM 2004)*, 2004, pp. 115–116.
- [3] Ari T. Alastalo and Ville Kaajakari, “Designing Capacitively Coupled Microelectromechanical Filters,” in *IEEE International Ultrasonics Symposium*, 2005, pp. 1588–1591.
- [4] Ville Kaajakari, Ari T. Alastalo, and Tomi Mattila, “Electrostatic transducers for micromechanical resonators: free space and solid dielectric,” *IEEE Trans. Ultrason., Ferroelect., Freq. Contr.*, 2006, in press.
- [5] John R. Vig, “Introduction to Quartz Frequency Standards,” <http://www.ieee-uffc.org/freqcontrol/quartz/vig/vigtoc.htm>, 1992.
- [6] Robert Weigel, David P. Morgan, John M. Owens, Arthur Ballato, Kenneth M. Lakin, Ken-ya Hashimoto, and Clemens C. W. Ruppel, “Microwave Acoustic Materials, Devices, and Applications,” *IEEE Trans. Microwave Theory Tech.*, vol. 50, no. 3, pp. 738–749, 2002.
- [7] Markku Ylilammi, Juha Ellä, Meeri Partanen, and Jyrki Kaitila, “Thin Film Bulk Acoustic Wave Filter,” *IEEE Trans. Ultrason., Ferroelect., Freq. Contr.*, vol. 49, no. 4, pp. 535–539, 2002.
- [8] V. Kaajakari, T. Mattila, A. Oja, J. Kiihamäki, and H. Seppä, “Square-Extensional Mode Single-Crystal Silicon Micromechanical Resonator for Low Phase Noise Oscillator Applications,” *IEEE Electron Device Lett.*, vol. 25, no. 4, pp. 173–175, 2004.
- [9] Peter Gammel, Georg Fischer, and Jérémie Bouchaud, “RF MEMS and NEMS Technology, Devices, and Applications,” *Bell Labs Technical Journal*, vol. 10, no. 3, pp. 29–59, 2005.
- [10] S. Lucyszyn, “Review of radio frequency microelectromechanical systems technology,” *IEE Proc.-Sci. Meas. Technol.*, vol. 151, no. 2, pp. 93–103, 2004.

- [11] Tauno Vähä-Heikkilä, “MEMS tuning and matching circuits, and millimeter wave on-wafer measurements,” D.Sc. thesis, Helsinki University of Technology, 2006, VTT Publications 596, Espoo 2006.
- [12] Siavash Pourkamali and Farrokh Ayazi, “Electrically Coupled MEMS Bandpass Filters: Part I: With Coupling Element,” *Sensors and Actuators A*, vol. 122, no. 2, pp. 307–316, 2005.
- [13] Siavash Pourkamali and Farrokh Ayazi, “Electrically Coupled MEMS Bandpass Filters: Part II: Without Coupling Element,” *Sensors and Actuators A*, vol. 122, no. 2, pp. 317–325, 2005.
- [14] Hengky Chandralahim, Dana Weinstein, Lih Feng Cheow, and Sunil A. Bhawe, “Channel-Select Micromechanical Filters Using High-K Dielectrically Transduced MEMS Resonators,” in *IEEE International Conference on Micro Electro Mechanical Systems, (MEMS 2006)*, 2006, pp. 894–897.
- [15] Clark T.-C. Nguyen, “Frequency-Selective MEMS for Miniaturized Low-Power Communication Devices,” *IEEE Trans. Microwave Theory Tech.*, vol. 47, no. 8, pp. 1486–1503, 1999.
- [16] Liwei Lin, Roger T. Howe, and Albert P. Pisano, “Microelectromechanical Filters for Signal Processing,” *J. Microelectromech. Syst.*, vol. 7, no. 3, pp. 286–294, 1998.
- [17] Milton Feng, Shyh-Chiang Shen, David C. Caruth, and Jian-Jang Huang, “Device Technologies for RF Front-End Circuits in Next-Generation Wireless Communications,” *Proc. IEEE*, vol. 92, no. 2, pp. 354–375, 2004.
- [18] Harrie A C Tilmans, Walter De Raedt, and Eric Beyne, “MEMS for wireless communications: ‘from RF-MEMS components to RF-MEMS-SiP’,” *J. Micromech. Microeng.*, vol. 13, pp. S139–S163, 2003.
- [19] Hee-Gook Lee, Jae Yeong Park, Jong Uk Bu, and Youngjoo Yee, “MEMS Technology for Advanced Telecommunication Applications,” *International Journal of High Speed Electronics and Systems*, vol. 12, no. 2, pp. 215–233, 2002.
- [20] J Jason Yao, “RF MEMS from a device perspective,” *J. Micromech. Microeng.*, vol. 10, pp. R9–R38, 2000.
- [21] Vijay K. Varadan, K. J. Vinoy, and K. A. Jose, *RF MEMS and Their Applications*, John Wiley & Sons Ltd, 2003.
- [22] Gabriel M. Rebeiz, *RF MEMS, Theory, Design, and Technology*, John Wiley & Sons, Inc., 2003.

- [23] Stephen Lewis, Susan Alie, Dr. Timothy Brosnihan, Craig Core, Teresa Core, Dr. Roger Howe, John Geen, David Hollocher, Dr. Michael Judy, Jack Memishian, Kieran Nunan, Dr. Richard Paine, Steven Sherman, Bob Tsang, and Bruce Wachtmann, “Integrated Sensor and Electronics Processing for $>10^8$ ”iMEMS” Inertial Measurement Unit Components,” in *IEEE International Electron Device Meeting (IEDM’03)*, 2003, pp. 39.1.1–39.1.4.
- [24] D. F. Moore and R. R. A. Syms, “Recent developments in micromachined silicon,” *Electronics & Communication Engineering Journal*, vol. 11, no. 6, pp. 261–270, 1999.
- [25] A. Bruce Carlson, Paul B. Crilly, and Janet C. Rutledge, *Communication Systems*, McGraw-Hill, 4th edition, 2002.
- [26] Heikki Seppä, Jukka Kyynäräinen, and Aarne Oja, “Microelectromechanical Systems in Electrical Metrology,” *IEEE Trans. Instrum. Meas.*, vol. 50, no. 2, pp. 440–444, 2001.
- [27] Luis Fernández, Javier Sesé, Remco Wiegerink, Jaap Flokstra, Henri Jansen, and Miko Elwenspoek, “Radio Frequency Power Sensor Based on MEMS Technology with Ultra Low Losses,” in *IEEE International Conference on Micro Electro Mechanical Systems, (MEMS 2005)*, 2005, pp. 191–194.
- [28] Ark-Chew Wong and Clark T.-C. Nguyen, “Micromechanical Mixer-Filters (“Mixlers”),” *J. Microelectromech. Syst.*, vol. 13, no. 1, pp. 100–112, 2004.
- [29] Clark T.-C. Nguyen, “Method and apparatus for generating a signal having at least one desired output frequency utilizing a bank of vibrating micromechanical devices,” United States Patent 6,577,040, 2003.
- [30] B.P. Otis, Y.H. Chee, R. Lu, N.M. Pletcher, and J.M. Rabaey, “An Ultra-Low Power MEMS-Based Two-Channel Transceiver for Wireless Sensor Networks,” in *Symposium On VLSI Circuits*, 2004, pp. 20–23.
- [31] L. D. Landau and E. M. Lifshitz, *Mechanics*, Butterworth-Heinemann, 1999.
- [32] V. Kaajakari, T. Mattila, A. Oja, and H. Seppä, “Nonlinear Limits for Single-Crystal Silicon Microresonators,” *J. Microelectromech. Syst.*, vol. 13, no. 5, pp. 715–724, 2004.
- [33] Sunil A. Bhawe, Di Gao, Roya Maboudian, and Roger T. Howe, “Fully-Differential Poly-SiC Lamé-Mode Resonator and Checkerboard Filter,” in *IEEE International Conference on Micro Electro Mechanical Systems, (MEMS 2005)*, 2005, pp. 223–226.

- [34] T. Mattila, J. Kiihamäki, T. Lamminmäki, O. Jaakkola, P. Rantakari, A. Oja, H. Seppä, H. Kattelus, and I. Tittonen, “12 MHz Micromechanical Bulk Acoustic Mode Oscillator,” *Sensors and Actuators A*, vol. 101, no. 1-2, pp. 1–9, 2002.
- [35] T. Mattila, O. Jaakkola, J. Kiihamäki, J. Karttunen, T. Lamminmäki, P. Rantakari, A. Oja, H. Seppä, H. Kattelus, and I. Tittonen, “14 MHz Micromechanical Oscillator,” *Sensors and Actuators A*, vol. 97-98, pp. 497–502, 2002.
- [36] M. Agarwal, K. K. Park, M. Hopcroft, S. Chandorkar, R. N. Candler, B. Kim, R. Melamud, G. Yama, B. Murmann, and T. W. Kenny, “Effects of Mechanical Vibrations and Bias Voltage Noise on Phase Noise of MEMS Resonator Based Oscillators,” in *IEEE International Conference on Micro Electro Mechanical Systems, (MEMS 2006)*, 2006, pp. 154–157.
- [37] Sheng-Shian Li, Yu-Wei Lin, Yuan Xie, Zeying Ren, and Clark T.-C. Nguyen, “Micromechanical ”Hollow-Disk” Ring Resonators,” in *17th International IEEE Conference on Micro Electro Mechanical Systems, (MEMS 2004)*, 2004, pp. 821–824.
- [38] Emmanuel P. Quévy, Alvaro San Paulo, Erol Basol, Roger T. Howe, Tsu-Jae King, and Jeffrey Bokor, “Back-End-of-Line Poly-SiGe Disk Resonators,” in *IEEE International Conference on Micro Electro Mechanical Systems, (MEMS 2006)*, 2006, pp. 234–237.
- [39] Jing Wang, Zeying Ren, and Clark T.-C. Nguyen, “1.156-GHz Self-Aligned Vibrating Micromechanical Disk Resonator,” *IEEE Trans. Ultrason., Ferroelect., Freq. Contr.*, vol. 51, no. 12, pp. 1607–1628, 2004.
- [40] Jing Wang, James E. Butler, Tatyana Feygelson, and Clark T.-C. Nguyen, “1.51 GHz Nanocrystalline Diamond Micromechanical Disk Resonator With Material-Mismatched Isolating Support,” in *International IEEE Conference on Micro Electro Mechanical Systems, (MEMS 2004)*, pp. 641–644.
- [41] Florian W Beil, Laura Pescini, Eva Höhberger, Andreas Kraus, Artur Erbe, and Robert H Blick, “Comparing schemes of displacement detection and subharmonic generation in nanomachined mechanical resonators,” *Nanotechnology*, vol. 14, pp. 799–802, 2003.
- [42] Jaume Verd, G. Abadal, J. Teva, María Villarroya Gaudó, Arantxa Uranga, Xavier Borrisé, Francesca Campabadal, Jaume Esteve, Eduardo Figueras Costa, Francesc Pérez-Murano, Zachary J. Davis, Esko Forsén, Anja Boisen, and Nuria Barniol, “Design, Fabrication, and Characterization of a Sub-microelectromechanical Resonator With Monolithically Integrated CMOS

- Readout Circuit,” *J. Microelectromech. Syst.*, vol. 14, no. 3, pp. 508–519, 2005.
- [43] Harrie A C Tilmans, “Equivalent circuit representation of electromechanical transducers: I. Lumped-parameter systems,” *J. Micromech. Microeng.*, vol. 6, pp. 157–176, 1996.
 - [44] A Q Liu, M Tang, A Agarwal, and A Alphones, “Low-loss lateral micromachined switches for high frequency applications,” *J. Micromech. Microeng.*, vol. 15, pp. 157–167, 2005.
 - [45] Seong-Dae Lee, Byoung-Chul Jun, Sam-Dong Kim, and Jin-Koo Rhee, “A Novel Pull-Up Type RF MEMS Switch With Low Actuation Voltage,” *IEEE Microwave Wireless Compon. Lett.*, vol. 15, no. 12, pp. 856–858, 2005.
 - [46] Jaewoo Lee, Chan Han Je, Sungweon Kang, and Chang-Auck Choi, “A Low-Loss Single-Pole Six-Throw Switch Based on Compact RF MEMS Switches,” *IEEE Trans. Microwave Theory Tech.*, vol. 53, no. 11, pp. 3335–3344, 2005.
 - [47] Hee-Chul Lee, Jae-Hyoung Park, Jae-Yeong Park, Hyo-Jin Nam, and Jong-Uk Bu, “Design, fabrication and RF performances of two different types on piezoelectrically actuated Ohmic MEMS switches,” *J. Micromech. Microeng.*, vol. 15, pp. 2098–2104, 2005.
 - [48] Meichun Ruan and Charles B. Wheeler, “Latching Micromagnetic Relays,” *J. Microelectromech. Syst.*, vol. 10, no. 4, pp. 511–517, 2001.
 - [49] Il-Joo Cho, Taeksang Song, Sang-Hyun Baek, and Euisik Yoon, “A Low-Voltage and Low-Power RF MEMS Series and Shunt Switches Actuated by Combination of Electromagnetic and Electrostatic Forces,” *IEEE Trans. Microwave Theory Tech.*, vol. 53, no. 7, pp. 2450–2457, 2005.
 - [50] Daniel Saias, Philippe Robert, Samuel Boret, Christophe Billard, Guillaume Bouche, Didier Belot, and Pascal Ancey, “An Above IC MEMS RF Switch,” *IEEE J. Solid-State Circuits*, vol. 38, no. 12, pp. 2318–2324, 2003.
 - [51] Brett Piekarski, Don DeVoe, Madan Dubey, Roger Kaul, and John Conrad, “Surface micromachined piezoelectric resonant beam filters,” *Sensors and Actuators A*, vol. 91, pp. 313–320, 2001.
 - [52] B. Antkowiak, J.P. Gorman, M. Varghese, D.J.D. Carter, and A.E. Duwel, “Design of a High-Q, Low-Impedance, GHz-Range Piezoelectric MEMS Resonator,” in *The 12th International Conference on Solid State Sensors, Actuators and Microsystems, (Transducers’03)*, 2003, pp. 841–846.

- [53] Gianluca Piazza, Reza Abdolvand, and Farrokh Ayazi, “Voltage-tunable piezoelectrically-transduced single-crystal silicon resonators on SOI substrate,” in *16th IEEE International Conference on Micro Electro Mechanical Systems, (MEMS 2003)*, 2003, pp. 149–152.
- [54] Le Yan, Jian Wu, and William C. Tang, “A 1.14 GHz Piezoelectrically Transduced Disk Resonator,” in *18th IEEE International Conference on Micro Electro Mechanical Systems, (MEMS 2005)*, 2005, pp. 203–206.
- [55] Arthur Erbe and Robert H. Blick, “Silicon-on-Insulator Based Nanoresonators for Mechanical Mixing at Radio Frequencies,” *IEEE Trans. Ultrason., Ferroelect., Freq. Contr.*, vol. 49, no. 8, pp. 1114–1117, 2002.
- [56] Tarik Bourouina, Amalia Garnier, and Hiroyuki Fujita, “Effect of direct current bias field and alternating current excitation field on vibration amplitudes and resonance frequencies of a magnetostrictively actuated bimorph microresonator,” *J. Appl. Phys.*, vol. 91, no. 1, pp. 112–120, 2002.
- [57] Robert B. Reichenbach, Maxim Zalalutdinov, Keith L. Aubin, Richard Rand, Brian H. Houston, Jeevak M. Parpia, and Harold G. Craighead, “Third-Order Intermodulation in a Micromechanical Thermal Mixer,” *J. Microelectromech. Syst.*, vol. 14, no. 6, pp. 1244–1252, 2005.
- [58] Sunil A. Bhave and Roger T. Howe, “Internal Electrostatic Transduction for Bulk-Mode MEMS Resonators,” in *Solid State Sensor, Actuator and Microsystems Workshop*, Hilton Head, SC, 2004, pp. 59–60.
- [59] Sunil A. Bhave and Roger T. Howe, “Silicon nitride-on-silicon bar resonator using internal electrostatic transduction,” in *The 13th International Conference on Solid-State Sensors, Actuators and Microsystems, (Transducers’05)*, 2005, pp. 2139–2142.
- [60] William C. Tang, Tu-Cuong H. Nguyen, and Roger T. Howe, “Laterally Driven Polysilicon Resonant Microstructures,” in *IEEE Conference on Micro Electro Mechanical Systems*, 1989, pp. 53–59.
- [61] John R. Reitz, Frederick J. Milford, and Robert W. Christy, *Foundations of Electromagnetic Theory*, Addison Wesley, 3rd edition, 1980.
- [62] L. Castañer, J. Pons, R. Nadal-Guardia, and A. Rodríguez, “Analysis of the extended operation range of electrostatic actuators by current-pulse drive,” *Sensors and Actuators A*, vol. 90, pp. 181–190, 2001.
- [63] Marc Madou, *Fundamentals of Microfabrication*, CRC Press, 1997.
- [64] Jyrki Kiihamäki, “Fabrication of SOI micromechanical devices,” D.Sc. thesis, Helsinki University of Technology, VTT Publications 559, Espoo 2005.

- [65] James M. Bustillo, Roger T. Howe, and Richard S. Muller, "Surface Micromachining for Microelectromechanical Systems," *Proc. IEEE*, vol. 86, no. 8, pp. 1552–1574, 1998.
- [66] N. Sepúlveda, D.M. Aslam, and J.P. Sullivan, "Polycrystalline Diamond RF MEMS Resonators with the Highest Quality Factors," in *IEEE International Conference on Micro Electro Mechanical Systems, (MEMS 2006)*, 2006, pp. 238–241.
- [67] Robert F. Wiser, Juyong Chung, Mehran Mehregany, and Christian A. Zorman, "Polycrystalline Silicon-Carbide Surface-Micromachined Vertical Resonators - Part I: Growth Study and Device Fabrication," *J. Microelectromech. Syst.*, vol. 14, no. 3, pp. 567–578, 2005.
- [68] Robert F. Wiser, Massood Tabib-Azar, Mehran Mehregany, and Christian A. Zorman, "Polycrystalline Silicon-Carbide Surface-Micromachined Vertical Resonators - Part II: Electrical Testing and Material Property Extraction," *J. Microelectromech. Syst.*, vol. 14, no. 3, pp. 579–589, 2005.
- [69] Hideki Takeuchi, Emmanuel Quévy, Sunil A. Bhawe, Tsu-Jae King, and Roger T. Howe, "Ge-Blade Damascene Process for Post-CMOS Integration of Nano-Mechanical Resonators," *IEEE Electron Device Lett.*, vol. 25, no. 8, pp. 529–531, 2004.
- [70] Christian A. Zorman and Mehran Mehregany, "Silicon Carbide for MEMS and NEMS - An Overview," in *Sensors 2002*, 2002, pp. 1109–1114.
- [71] Franz Laermer and Andrea Schilp, "Method for anisotropic plasma etching of substrates," United States Patent 5,498,312, 1996.
- [72] Siavash Pourkamali and Farrokh Ayazi, "Fully Single Crystal Silicon Resonators with Deep-Submicron Dry-Etched Transducer Gaps," in *IEEE International Conference on Micro Electro Mechanical Systems, (MEMS 2004)*, 2004, pp. 813–816.
- [73] Wan-Thai Hsu, John R. Clark, and Clark T.-C. Nguyen, "A sub-micron capacitive gap process for multiple-metal-electrode lateral micromechanical resonators," in *IEEE International Conference on Micro Electro Mechanical Systems, (MEMS 2001)*, 2001, pp. 349–352.
- [74] Siavash Pourkamali, Akinori Hashimura, Reza Abdolvand, Gavin K. Ho, Ahmet Erbil, and Farrokh Ayazi, "High-Q Single Crystal Silicon HARPSS Capacitive Beam Resonators With Self-Aligned Sub-100-nm Transduction Gaps," *J. Microelectromech. Syst.*, vol. 12, no. 4, pp. 487–496, 2003.

- [75] Emmanuel Quévy, Bernard Legrand, Dominique Collard, and Lionel Buchaillot, “Ultimate technology for micromachining of nanometric gap HF micromechanical resonators,” in *IEEE International Conference on Micro Electro Mechanical Systems, (MEMS 2003)*, 2003, pp. 157–160.
- [76] J. Kiihamäki, V. Kaajakari, H. Luoto, H. Kattelus, and M. Yli-Koski, “Fabrication of single crystal silicon resonators with narrow gaps,” in *The 13th International Conference on Solid-State Sensors, Actuators and Microsystems, (Transducers’05)*, 2005, pp. 1354–1357.
- [77] Kevin Y. Yasumura, Timothy D. Stowe, Eugene M. Chow, Timothy Pfaffman, Thomas W. Kenny, Barry C. Stipe, and Daniel Rugar, “Quality Factors in Micron- and Submicron-Thick Cantilevers,” *J. Microelectromech. Syst.*, vol. 9, no. 1, pp. 117–125, 2000.
- [78] Ron Lifshitz and M. L. Roukes, “Thermoelastic damping in micro- and nanomechanical systems,” *Phys. Rev. B*, vol. 61, no. 8, pp. 5600–5608, 2002.
- [79] V. Kaajakari, Jukka K. Koskinen, and Tomi Mattila, “Phase Noise in Capacitively Coupled Micromechanical Oscillators,” *IEEE Trans. Ultrason., Ferroelect., Freq. Contr.*, vol. 52, no. 12, pp. 2322–2331, 2005.
- [80] J. R. Vig and Yoonkee Kim, “Noise in Microelectromechanical System Resonators,” *IEEE Trans. Ultrason., Ferroelect., Freq. Contr.*, vol. 46, no. 6, pp. 1558–1565, 1999.
- [81] A. N. Cleland and M. L. Roukes, “Noise processes in nanomechanical resonators,” *J. Appl. Phys.*, vol. 92, no. 5, pp. 2758–2769, 2002.
- [82] B. Razavi, *RF Microelectronics*, Prentice Hall, 1998.
- [83] ETSI, “GSM global system for mobile communications,” TS 145 005 V6.11.0 (2005-09).
- [84] Reza Navid, John R. Clark, Mustafa Demirci, and Clark T.-C. Nguyen, “Third-order intermodulation distortion in capacitively-driven cc-beam micromechanical resonators,” in *IEEE International Conference on Micro Electro Mechanical Systems, (MEMS 2001)*, 2001, pp. 228–231.
- [85] T. Veijola and T. Mattila, “Modeling of Nonlinear Micromechanical Resonators and Their Simulation with the Harmonic-Balance Method,” *International Journal of RF and Microwave Computer Aided Engineering*, vol. 11, no. 5, pp. 310–321, 2001.
- [86] Jr. W. Weaver, S. Timoshenko, and D. Young, *Vibration Problems in Engineering*, Wiley, 5th edition, 1990.

- [87] T. Lee, *The Design of CMOS Radio-Frequency Integrated Circuits*, Cambridge University Press, 1998.
- [88] Leonhard M. Reindl, Alfred Pohl, Gerd Scholl, and Robert Weigel, "SAW-Based Radio Sensor Systems," *IEEE Sensors J.*, vol. 1, no. 1, pp. 69–78, 2001.
- [89] Ram M. Narayanan, Wei Zhou, Kelvin H. Wagner, and Sangtaek Kim, "Acoustooptic Correlation Processing in Random Noise Radar," *IEEE Geosci. Remote Sensing Lett.*, vol. 1, no. 3, pp. 166–170, 2004.
- [90] Leonhard Reindl, Clemens C. W. Ruppel, Stefan Berek, Ulrich Knauer, Martin Vossiek, Patric Heide, and Lutz Oréans, "Design, Fabrication, and Application of Precise SAW Delay Lines Used in an FMCW Radar System," *IEEE Trans. Microwave Theory Tech.*, vol. 49, no. 4, pp. 787–794, 2001.
- [91] S. K. Salmon, "Practical Aspects of Surface-Acoustic-Wave Oscillators," *IEEE Trans. Microwave Theory Tech.*, vol. MTT-27, no. 12, pp. 1012–1018, 1979.
- [92] Thomas E. Parker and Gary K. Montress, "Precision Surface-Acoustic-Wave (SAW) Oscillators," *IEEE Trans. Ultrason., Ferroelect., Freq. Contr.*, vol. 35, no. 3, pp. 342–364, 1988.
- [93] D. Ciplys, R. Rimeika, A. Sereika, R. Gaska, M.S. Shur, J.W. Yang, and M.A. Khan, "GaN-based SAW delay-line oscillator," *Electronics Letters*, vol. 37, no. 8, pp. 545–546, 2001.
- [94] J. H. Yin, K. X. Shen, Y. Shui, Z. L. Jiang, and S. P. He, "Modified SAW Diode Convolver," *Electronics Letters*, vol. 28, no. 2, pp. 172–174, 1992.
- [95] Shiwei Zhao, Huaping Liu, and Zhi Tian, "A Decision-Feedback Autocorrelation Receiver for Pulsed Ultra-Wideband Systems," in *Proc. IEEE Radio and Wireless Conference*, 2004, pp. 251–254.
- [96] D. M. Pozar, *Microwave Engineering*, Wiley, 2nd edition, 1998.
- [97] B. A. Auld, *Acoustic Fields and Waves in Solids*, Krieger, 2nd edition, 1990.
- [98] H. F. Pollard, *Sound Waves in Solids*, Pion Ltd., 1977.
- [99] Neil W. Ashcroft and N. David Mermin, *Solid State Physics*, Saunders College Publishing, 1976.
- [100] Simon Ramo, John R. Whinnery, and Theodore Van Duzer, *Fields and Waves in Communication Electronics*, John Wiley & Sons, 2nd edition, 1984.

APPENDIX 1

Electromechanical Instability

Electromechanical Instability

Increasing the bias voltage enhances the electrostatic coupling and lowers the typically very high impedance level of the MEMS resonator thus reducing insertion loss from a low-impedance source such as a $50\text{-}\Omega$ generator. As shown in (22 c), the voltage bias also lowers the effective spring constant of the resonator. For large-enough bias, the resonator becomes unstable and is deflected against one of the stationary transducer electrodes (pull-in).

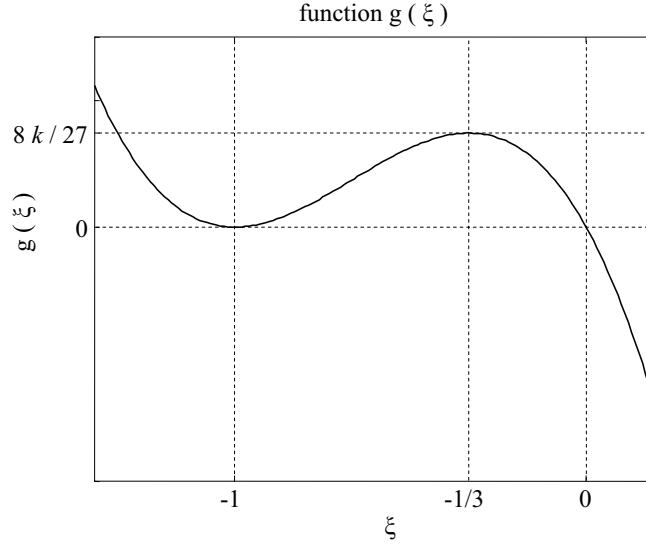


Figure 1: Function $g(\xi)$ in (2).

The pull-in voltage can be obtained as follows. For the single-transducer structure of Fig. 8 (a), the equation of motion with zero AC voltage becomes using (23 a)

$$m\ddot{x} + \gamma\dot{x} + kx = F_1 \Rightarrow m\ddot{\xi} + \gamma\dot{\xi} = -\frac{1}{2} \frac{k_e}{(1+\xi)^2} - k\xi. \quad (1)$$

Solving for the rest position ($\dot{\xi} = 0$ and $\ddot{\xi} = 0$), one obtains

$$k_e = -2k\xi(1+\xi)^2 \equiv g(\xi). \quad (2)$$

The function $g(\xi)$ is plotted in Fig. 1. One sees that if $k_e > 8k/27$, there is no solution for the resonator displacement inside the transducer gap resulting in pull-in. The corresponding voltage (pull-in voltage) is given by (12 a). Similarly, for the double-transducer circuit of Fig. 8 (c), one obtains the instability at a higher bias voltage of (12 b).

APPENDIX 2

Derivation of the Equivalent Circuits

Derivation of the Equivalent Circuits

To derive the small-signal electrical-equivalent circuit of Fig. 8 (c), we assume a harmonic excitation $u = u_0 e^{j\omega t}$ that yields $\dot{u} = j\omega u$. For the load voltage $u_L = i_2 Z_L$ and for the voltage across the source resistance $u_s = i_1 R_{ac}$, we also use $\dot{u}_L = j\omega u_L$ and $\dot{u}_s = j\omega u_s$, respectively. Equations (23 a), (23 b), (24 a) and (24 b) for the forces and currents are now approximated to first order in the small parameters $\xi \equiv x/d$, $\bar{u} \equiv u/V$ and $\bar{u}_L \equiv u_L/V$ resulting in

$$i_1 = (j\omega C_0 u - \eta \dot{x}) / (1 + j\omega C_0 R_{ac}) = u/Z \quad (1a)$$

$$i_2 = \eta \dot{x} / (1 + j\omega C_0 Z_L) \quad (1b)$$

$$F_1 = -\eta(V/2 + u') + k_e x - \gamma_s \dot{x} \quad (1c)$$

$$F_2 = \eta V/2 + k_e x - \gamma_L \dot{x}, \quad (1d)$$

where Z is the unknown input impedance, $\gamma_s \equiv \eta^2(Z_0 || R_{ac})$ and $\gamma_L \equiv \eta^2(Z_0 || Z_L)$ are the complex dissipation coefficients introduced by the source and load impedances and $u' = u/(1 + j\omega C_0 R_{ac})$ is the Thévenin-equivalent AC voltage. The equation of motion for the resonator ($m\ddot{x} + \hat{\gamma}\dot{x} + \bar{k}x = F_1 + F_2$) can now be written as

$$m\ddot{x} + \hat{\gamma}\dot{x} + \bar{k}x = -\eta u', \quad (2)$$

where $\hat{\gamma} \equiv \gamma + \gamma_s + \gamma_L$ and $\bar{k} \equiv k - 2k_e$. Solving now, as usual, for the resonator motion by assuming $x = Ae^{j\omega t}$, where A is an unknown complex amplitude, one obtains the resonator velocity as

$$\dot{x} = \frac{-j\omega\eta u'}{\bar{k} - m\omega^2 + j\omega\hat{\gamma}}. \quad (3)$$

Inserting (3) into (1 a) one finds the input impedance Z as shown in Fig. 8 (d)

$$Z = R_{ac} + Z_0 || (Z_{em} - (Z_0 || R_{ac})), \quad (4)$$

where

$$\begin{aligned} Z_{em} &= \frac{\bar{k} - m\omega^2 + j\omega\hat{\gamma}}{j\omega\eta^2} = \frac{\gamma}{\eta^2} + j\omega\frac{m}{\eta^2} + \frac{1}{j\omega\frac{\eta^2}{\bar{k}}} + (Z_0 || R_{ac}) + (Z_0 || Z_L) \\ &= R_m + j\omega L_m + \frac{1}{j\omega C_{m,2}} + (Z_0 || R_{ac}) + (Z_0 || Z_L). \end{aligned} \quad (5)$$

Here R_m , L_m and $C_{m,2}$ are given by (22 a), (22 b) and (22 c), respectively. Similarly, one can derive the equivalent circuit of Fig. 8 (b).

Author(s) Alastalo, Ari			
Title Microelectromechanical Resonator-Based Components for Wireless Communications Filters and Transmission Lines			
Abstract <p>Starting in the early 1960's, when the integrated-circuit (IC) technology was developed, micromachining and microelectromechanical systems (MEMS) have grown into a broad research field with several commercial successes. Typical applications of MEMS are in physical, chemical and biochemical sensors, as well as in optical systems such as the digital micromirror device of Texas Instruments. From the 1990's, the advances in the processing technologies and the tremendous growth of the wireless-communication market have drawn much interest into radio-frequency MEMS devices (RF MEMS) such as filters, oscillators, switches and tunable capacitors. These are now beginning to penetrate the market.</p> <p>This thesis considers electrostatically-actuated RF-MEMS filters and delay lines. For filters, the work concentrates on nonlinear distortion and filter design. The intermodulation properties of capacitively-coupled MEMS filters are analytically solved in closed form and the theory is verified in numerical simulations as well as in measurements with MEMS resonators. The analysis is more generally valid than the previously published results. The theory is utilized to formulate a design procedure for MEMS filters that, for the first time, takes systems specifications for tolerable intermodulation distortion and insertion-loss into account. For delay lines, capacitive actuation of bulk-acoustic waves in a solid rod is analyzed. In particular, challenges in impedance matching due to the weakness of the electrostatic coupling are quantified. Finally, a new kind of resonator-chain delay line for high-frequency (HF) signals is introduced. This delay line is characterized by extremely slow signal group velocity ($\sim 10\text{--}100\text{ m/s}$), narrow-band response, and much lower characteristic impedance than found for the solid-rod waveguide enabling efficient signal coupling. Properties of the resonator-chain waveguide are theoretically analyzed and the results are verified in measurements of fabricated devices.</p>			
Keywords MEMS, radio-frequency MEMS, microelectromechanical filters, microelectromechanical resonators, components, transducers, wireless communication, transmission lines, acoustic wave propagation, intermodulation			
ISBN 951-38-6865-6 (soft back ed.) 951-38-6866-4 (URL: http://www.vtt.fi/publications/index.jsp)			
Series title and ISSN VTT Publications 1235-0621 (soft back ed.) 1455-0849 (URL: http://www.vtt.fi/publications/index.jsp)			Project number
Date October 2006	Language English, finnish abstr.	Pages 57 p. + app. 56 p.	Price C
Name of project MIRA		Commissioned by	
Contact VTT Technical Research Centre of Finland P.O. Box 1000, FI-02044 VTT, Finland Phone internat. +358 20 722 111 Fax +358 20 722 7012		Sold by VTT Technical Research Centre of Finland P.O.Box 1000, FI-02044 VTT, Finland Phone internat. +358 20 722 4404 Fax +358 20 722 4374	

Tekijä(t)

Alastalo, Ari

Nimeke

Mikromekaanisiin resonaattoreihin perustuvat komponentit langattoman tiedonsiirron sovelluksissa Suodattimet ja siirtolinjat

Tiivistelmä

Mikroelektromekaanisten järjestelmien (MEMS) kehitys alkoi 1960-luvun alussa yhdessä integroitujen piirien (IC) teknologian kanssa. Tähän päivään mennessä mikromekaniikka on kehittynyt laajaksi tutkimusalaksi ja johtanut useisiin kaupallisiin menestyksiin. MEMS-teknologiaa sovelletaan mm. fysikaalisissa, kemiallisissa ja biokemiallisissa antureissa sekä optisissa järjestelmissä, kuten Texas Instrumentsin mikropileissä, joita käytetään videoprojektoreissa. Kiinnostus radiotaajuisiin MEMS-komponentteihin (RF MEMS) on lisääntynyt voimakkaasti 1990-luvun alusta alkaen valmistusteknologian ja langattoman tiedonsiirron markkinoiden kehityksen myötä. Radiotekniikassa MEMS-teknologiaa pyritään soveltamaan mm. suodattimissa, oskillaattoreissa, kytkimissä ja säädettävissä kondensaattoreissa. Ensimmäiset tällaiset komponentit ovat jo kaupallistuneet.

Tässä väitöskirjassa käsitellään kapasitiivisesti kytkettyjä RF-MEMS-suodattimia ja viivelinjoja. Suodattimien osalta työ keskittyy epälineaarisuuksien ja häviöiden huomioimiseen suodinsuunnittelussa. MEMS-suodinten intermodulaatio-ominaisuudet ratkaistaan työssä analyyttisesti aikaisempaa yleisemmin ja saadut tulokset varmennetaan tietokonesimulaatioissa ja mittauksissa. Tulosten pohjalta laaditaan MEMS-suodinsuunnittelulle säännöt, joissa otetaan ensimmäistä kertaa huomioon asetetut vaatimukset sekä intermodulaatiolle että häviöille. Viivelinjojen osalta työssä käsitellään mikromekaaniseen tankoon perustuvaa tilavuusaaltoviivelinjaa ja tuodaan esiin vaikeudet, jotka liittyvät riittävän hyvän kytkennän saavuttamiseen tällaisessa rakenteessa. Tehokkaampi kytkentä on HF-taajuuksilla mahdollinen jousimassaketjuun perustuvaan viivelinjaan, jollainen esitellään ja analysoidaan tässä väitöstyössä. Hyvän kytkennän lisäksi tämän viivelinjan ominaisuuksiin kuuluu kapeakaistaisuus ja erittäin hidas signaalin kulkunopeus. Mikromekaanisen jousimassaketjuviivelinjan toiminta varmennetaan mittauksin.

Avainsanat

MEMS, radio-frequency MEMS, microelectromechanical filters, microelectromechanical resonators, components, transducers, wireless communication, transmission lines, acoustic wave propagation, intermodulation

ISBN

951-38-6865-6 (nid.)

951-38-6866-4 (URL: <http://www.vtt.fi/publications/index.jsp>)

Avainnimeke ja ISSN

VTT Publications

1235-0621 (nid.)

1455-0849 (URL: <http://www.vtt.fi/publications/index.jsp>)

Projektinnumero

Julkaisuaika

Lokakuu 2006

Kieli

Englanti, suom. tiiv.

Sivuja

57 s. + liitt. 56 s.

Hinta

C

Projektin nimi

MIRA

Toimeksiantaja(t)

Yhteystiedot

VTT,
PL 1000, 02044 VTT
Puh. vaihde 020 722 111
Faksi 020 722 7012

Myynti

VTT
PL 1000, 02044 VTT
Puh. 020 722 4404
Faksi 020 722 4374

Starting in the early 1960's, when the integrated-circuit (IC) technology was developed, micromachining and microelectromechanical systems (MEMS) have grown into a broad research field with several commercial successes. Typical applications of MEMS are in physical, chemical and biochemical sensors, as well as in optical systems such as the digital micromirror device of Texas Instruments. From the 1990's, the advances in the processing technologies and the tremendous growth of the wireless-communication market have drawn much interest into radio-frequency MEMS devices (RF MEMS) such as filters, oscillators, switches and tunable capacitors. This thesis considers electrostatically-actuated RF-MEMS filters and delay lines. The intermodulation properties of capacitively-coupled MEMS filters are analytically solved in closed form and the theory is verified in numerical simulations as well as in measurements with MEMS resonators. The theory is utilized to formulate a design procedure for MEMS filters that takes systems specifications for tolerable intermodulation distortion and insertion-loss into account. For delay lines, capacitive actuation of bulk-acoustic waves in a solid rod is analyzed. In particular, challenges in impedance matching due to the weakness of the electrostatic coupling are quantified. Finally, a new kind of resonator-chain delay line is introduced. This delay line is characterized by record-low acoustic signal velocity, narrow-band response, and much lower characteristic impedance than found for the solid-rod waveguide enabling efficient signal coupling.

Tätä julkaisua myy	Denna publikation säljs av	This publication is available from
VTT PL 1000 02044 VTT Puh. 020 722 4404 Faksi 020 722 4374	VTT PB 1000 02044 VTT Tel. 020 722 4404 Fax 020 722 4374	VTT P.O. Box 1000 FI-02044 VTT, Finland Phone internat. +358 20 722 4404 Fax +358 20 722 4374